An Intercomparison of Cloud-Resolving Models with the ARM Summer 1997 IOP Data

Kuan-Man Xu[1], Richard T. Cederwall[2], Leo J. Donner[3],
Wojciech W. Grabowski[4], Francoise Guichard[5], Daniel E. Johnson[6],
Marat Khairoutdinov[7], Steven K. Krueger[8], Jon C. Petch[9],
David A. Randall[7], Charles J. Seman[3], Wei-Kuo Tao[6],
Donghai Wang[10,1], Shao Cheng Xie[2], J. John Yio[2], and
Ming-Hua Zhang[11]

[1] NASA Langley Research Center, Hampton, VA, USA
[2] Lawrence Livermore National Laboratory, Livermore, CA, USA
[3] NOAA Geophysical Fluid Dynamics Laboratory, Princeton, NJ, USA
[4] National Center for Atmospheric Research, Boulder, CO, USA
[5] Centre National de Recherches Meteorologiques, France
[6] NASA Goddard Space Flight Center, Greenbelt, MD, USA
[7] Colorado State University, Fort Collins, CO, USA
[8] University of Utah, Salt Lake City, UT, USA
[9] The Met Office, Bracknell, UK
[10] Hampton University, Hampton, VA, USA
[11] State University of New York, Stony Brook, NY, USA

Submitted to
Quarterly Journal of the Royal Meteorological Society

January 19, 2001
Revised September 17, 2001

Corresponding author address:
Dr. Kuan-Man Xu
Mail Stop 420
NASA Langley Research Center
Hampton, VA 23681
E-mail: k.m.xu@larc.nasa.gov

Summary

This paper reports an intercomparison study of midlatitude continental cumulus convection simulated by eight 2-D and two 3-D cloud resolving models (CRMs), driven by observed large-scale advective temperature and moisture tendencies, surface turbulent fluxes, and radiative heating profiles during three subperiods of the Summer 1997 Intensive Observation Period (IOP) of the U.S. Department of Energy's Atmospheric Radiation Measurement (ARM) program. Each subperiod includes two or three precipitation events of various intensities over a span of 4 or 5 days. The results can be summarized as follows.

CRMs can reasonably simulate midlatitude continental summer convection observed at the ARM Cloud and Radiation Testbed (CART) site in terms of the intensity of convective activity, and the temperature and specific humidity evolution. Delayed occurrences of the initial precipitation events are a common feature for all three subcases among the models. Cloud mass fluxes, condensate mixing ratios and hydrometeor fractions produced by all CRMs are similar. Some of the simulated cloud properties such as cloud liquid water path and hydrometeor fraction are rather similar to available observations. All CRMs produce large downdraft mass fluxes with magnitudes similar to those of updrafts, in contrast with CRM results for tropical convection. Some intermodel differences in cloud properties are likely to be related to those in the parameterizations of microphysical processes.

There is generally a good agreement between the CRMs and observations with CRMs being significantly better than single-column models (SCMs), suggesting that current results are suitable for use in improving parameterizations in SCMs. However, improvements can still be made in the CRM simulations; those include the proper initialization of the CRMs and a more proper method of diagnosing cloud boundaries in model outputs for comparison with satellite and cloud radar observations.

Keywords: Cloud Resolving Models; Model Intercomparison Study; Continental Cumulus Convection

1. Introduction

Cloud-related processes occur on finer scales than those resolved by large-scale models. A subset of these models are the general circulation models (GCMs) used for weather forecast and climate studies. These models have to use parameterizations to represent these subgrid-scale cloud processes, for example, cumulus convection, cloud microphysics and cloud cover parameterizations. Improvements of GCMs rely heavily on the development of more physically-based parameterizations of cloud processes. It is the objective of the Global Energy and Water-cycle Experiment (GEWEX) Cloud System Study (GCSS) to develop new parameterizations of cloud-related processes for large-scale models (Browning 1994; Randall et al. 2001).

An important tool for achieving the GCSS objective, in addition to observational data, is fine-resolution numerical models such as large-eddy simulation (LES) and cloud resolving models (CRMs). Both allow an explicit treatment of fine-scale cloud dynamics and cloud systems. In fact, observations alone, though extremely valuable, cannot provide all the data needed for a thorough development and evaluation of many aspects of the parameterizations of cloud processes. For instance, cloud mass fluxes, which are central to many existing cumulus parameterizations, are very difficult to retrieve from observations. Therefore, LES and CRMs have been used to fill the gap between sparse observations and parameterization development (Randall et al. 1996) for an in-depth understanding of cloud-related processes, an essential step to the formulation of any advanced and physically sound parameterization of these processes.

Because LES and CRMs have their own subgrid-scale parameterizations and numerical uncertainties and there are no complete data set to verify the performance of all aspects of numerical simulations by these models, a standard approach that has been widely adopted in the community is the intercomparison study (e.g., Cess et al. 1989; Gates 1992; Moeng et al. 1996; Boyle et al. 2000; Ghan et al. 2000). In order to have a successful intercomparison study, high quality data are needed. In outlining the approach of the Precipitating Convective Cloud Systems Work-

ing Group (WG) of GCSS, i.e., WG 4, Moncrieff et al. (1997) concluded: "A comprehensive evaluation of state-of-the-art CRMs will require state-of-the-art observations." In particular, cloud property observations should be available for comparison, in addition to large-scale thermodynamic variables and radiative fluxes from the surface and the top of the atmosphere. Some recent field campaigns have provided increasingly more comprehensive observations of cloud properties, in particular, TOGA COARE[1] (Webster and Lucas 1992) and ARM[2] (Stokes and Schwartz 1994).

GCSS WG 4 conducted two case studies using TOGA COARE data: Case 1, two- and three-dimensional (3-D) modeling of a squall line on a time scale of a few hours (Redelsperger et al. 2000), and Case 2, two-dimensional (2-D) simulation of the evolution of convection under imposed large-scale conditions during TOGA COARE Intensive Observation Period (IOP; Krueger et al. 2001; Table 1). In a related research effort, the ARM Cloud Parameterization and Modeling (CPM) WG conducted a single-column model (SCM) intercomparison study of midlatitude summertime convection using the ARM July 1995 IOP data set (Ghan et al. 2000).

There have also been a few "long-term" simulations (i.e., over one-week period) using the same approach as in Case 2 intercomparison study (Table 1). Most of these studies focused on tropical convection using either the GATE[3] (Kuettner and Parker 1976) or TOGA COARE data set to conduct 2-D and sometimes 3-D CRM simulations. In these studies, the simulated thermodynamic profiles and characteristics of convective cloud systems can be compared with observations. However, the degree of consistency of cloud properties such as cloud mass fluxes and cloud liquid water paths between different models can only be investigated by an intercomparison study.

The present case, Case 3, a joint GCSS and ARM intercomparison project, is aimed at advancing the understanding of midlatitude continental convection. Case 3 compares the performance of two 3-D CRMs, eight 2-D CRMs and 15 SCMs by simulating cumulus convection

---

1. Tropical Ocean and Global Atmosphere (TOGA) Coupled Ocean-Atmosphere Response Experiment.
2. U.S. Department of Energy's Atmospheric Radiation Measurement (ARM) Program.
3. Global Atmospheric Research Program's Atlantic Tropical Experiment.

observed at the Southern Great Plains (SGP) Cloud and Radiation Testbed (CART) site during Summer 1997 IOP of the ARM program. A rich variety of cloud property observations are readily available. Most of the CRMs have, however, not been used to simulate midlatitude continental convection with an observed large-scale data set (Table 1). The unique aspects of this study are 1) the simulations of midlatitude continental convection and 2) the comparisons with more comprehensive cloud property observations than earlier intercomparison studies.

The goal of the present paper is to document the results of CRM simulations and the findings of the intercomparison, while the SCM part of the project is reported elsewhere (Xie et al. 2001). The specific objectives of this CRM intercomparison study are: 1) to compare the performance of CRMs in simulating midlatitude convection and 2) to evaluate CRM simulations with detailed cloud property observations. In addition, this work serves as a foundation for parameterization developers for using the large data set produced by CRMs to improve their parameterizations and for further work by contributing CRM groups to address many issues raised in this paper, in particular, some model deficiencies.

2. Description of CRMs and Design of Simulations

a. Description of CRMs

Eight groups participating in this intercomparison study perform simulations with 2-D (x and z) CRMs (Table 2). All 2-D models orient on the east-west direction. CSULEM and UKLEM (two subcases) groups also perform 3-D simulations. All of the model codes have been developed independently although some parts of the CRMs are rather similar between some models. Each model includes four major parts: cloud-scale dynamics, cloud microphysics, turbulence and radiation.

Most of the CRMs are based upon anelastic dynamics, which filters out the sound waves, except for the GFDL and LaRC CRMs which use the compressible dynamics. Two time steps are used in LaRC CRM (Xue et al. 2001), with the smaller time step for sound waves. The anelastic

5

dynamics allows for a larger time step (Table 3) for integration but needs to solve an elliptic equation for pressure. Periodic (cyclic) lateral boundary conditions are implemented in all models. Other details related to numerics are listed in Table 3.

Bulk cloud microphysical representations are used in all CRMs, with 4 or 5 water species (cloud water, cloud ice, rainwater, snow and graupel/hail; see Table 4). The majority of CRMs use some variations of the Lin et al. (1983) or Rutledge and Hobbs (1984) schemes, for example, CNRM, GCE, LaRC, UCLA/CSU and UKLEM. Other CRMs (CSULEM, GFDL and EULAG) have a fewer predicted water species with diagnostic partitionings between some condensate/ hydrometeor categories that depend upon the ambient temperature.

Turbulence parameterization is also an important component of CRMs. Two CRMs use first-order closure scheme of Smagorinsky (1963) and Lilly (1968; GFDL and UKLEM), five use one and a half-order prognostic turbulent kinetic energy (TKE) closure (CSULEM, EULAG, GCE, LaRC and CNRM), and one uses third-order closure (UCLA/CSU; see Table 5). Another related aspect of CRMs is the formulation of surface turbulent fluxes of heat, moisture and momentum. Although the domain-averaged fluxes are prescribed in all models (see section 2b), the impact of surface turbulent flux formulations on simulated cloud processes cannot be ignored because of the deep boundary layers over land. For the sake of brevity, details of these formulations are omitted.

The last important component of CRMs is the radiative transfer parameterization. Because radiative heating rate profiles are prescribed in this study, details of radiation parameterizations used in CRMs are omitted.

b. Design of simulations

Three simulations are run by each model; each corresponds to a subperiod of the ARM Summer 1997 IOP. In all simulations, the observed large-scale advective cooling and moistening rate profiles are imposed on the model gridpoints uniformly in the horizontal domain and continu-

ously in time. Because observations are available every 3 h, an interpolation of the observed profiles (advective forcings and wind components) to model time and height levels is required[4]. The domain-averaged horizontal wind components are nudged toward the observed horizontal wind components with a nudging time of 1 or 2 h (Grabowski et al. 1996; Xu and Randall 1996). The horizontal inhomogeneity of u and v components inside the CRM domain is preserved by the nudging procedure.

Also prescribed are the radiative heating rate profiles, based upon the European Center for Medium-range Weather Forecasting (ECMWF) forecast model (not shown) and adjusted by the observed column radiative fluxes[5]. This eliminates the complicated interactions between clouds and radiation and simplifies interpretation of the intercomparison results. The impact of interactive radiation is a focus of further studies from contributing groups (e.g., Xu and Randall 2000b).

Observed surface turbulent fluxes from Energy Balance/Bowen Ratio (EBBR) measurements are imposed to all models because most CRMs do not have a land-surface scheme so that the complicated land surface processes and their feedbacks to cloud processes are eliminated. In CRMs, however, only the domain-averaged fluxes are constrained to the observed values. The horizontal variations of the surface fluxes are retained, which are calculated from surface turbulent flux formulations using the prescribed ground temperature and soil wetness.

Table 6 lists the observed subperiod-mean column budget components. The column heat (dry static energy, s) and moisture (q_v) budgets of the atmosphere, neglecting the impact of local change of cloud liquid water, can be expressed as:

$$\int_0^\infty \rho \frac{\partial s}{\partial t} dz = \int_0^\infty \rho \left(\frac{\partial s}{\partial t}\right)_{LS} dz + SH + LP + c_p \int_0^\infty \rho Q_R dz \ , \tag{1}$$

---

4. Some models such as EULAG and LaRC CRMs only update the forcings every 3 h.
5. The top level of the prescribed heating rates is at 115 hPa. Thus, vertical interpolation to model vertical levels above 115 hPa can introduce an error in the net radiative flux as large as 10 W m^{-2}, depending upon the depth of the model.

$$\int\limits_0^\infty \rho \frac{\partial q_v}{\partial t} dz = \int\limits_0^\infty \rho \left(\frac{\partial q_v}{\partial t} \right)_{LS} dz + E - P \ , \tag{2}$$

where the left-hand-side terms of (1) and (2) are the heat and moisture storages, respectively, the first terms on the right-hand-side (RHS) are the large-scale advective tendencies, SH the sensible heat flux, E the surface evaporation rate, P the surface precipitation rate, and the last term on RHS of (1) is the radiative heating tendency. Table 6 shows that Subperiod A has the largest surface precipitation rate, large-scale advective moistening and heat storage among the subperiods. The remaining components have more comparable magnitudes among the subperiods.

In all models, convection is initiated by introducing small random perturbations in the temperature field (0.5 K maximum magnitude) in the subcloud layer of the initial sounding for the first hour or so, as in simulations of tropical convection (e.g., Krueger 1988). Use of small random perturbations to initiate convection for continental convection may not be an appropriate method, as further discussed in section 4b.

In summary, major differences in the design of simulations between Case 2 (Krueger et al. 2001) and Case 3 consist of 1) prescribing the radiative heating rate profiles, instead of interactive radiation, and 2) prescribing the domain-averaged surface turbulent fluxes of heat and moisture, instead of computing them from the prescribed land-surface temperature and soil wetness. The major advantage for Case 3 is, thus, that the simulated cloud processes are easily compared among the CRMs. However, the tightly constrained column budgets do not allow any feedback from the land surface and radiative processes to impact the simulated cloud processes. This issue will be addressed by some contributing groups in the near future.

3. Characteristics of Case 3

The ARM Summer 1997 IOP covers a 29-day period, starting from 2330 UTC on 18 June and ending at 2330 UTC on 17 July (Julian Day 170 to 199). Three subperiods of 4- to 5-day

durations (see the time series of surface precipitation[6] shown in Fig. 1) are chosen for the simulations. Each subperiod corresponds to a subcase of Case 3 (Table 7). These three short subperiods are selected to avoid the advection of large cloud systems into the ARM CART domain, but the advection of portions of some cloud systems frequently occurs. This impacts the simulated timing of precipitation events (see section 4b) and the magnitudes of some cloud properties (section 4d).

Balloon-borne soundings of winds, temperature and dewpoint temperature were obtained every 3 h from the ARM CART central facility located near Lamont, OK ($36.61°$ N, $97.49°$ W) and from four boundary facilities, which form a rectangle of approximate 300 x 370 km^2. The sounding/profiler data, combined with the surface and the top-of-the-atmosphere flux observations, are analyzed over such a horizontal domain representing a GCM grid box[7], using a constrained variational objective analysis method (Zhang and Lin 1997; Zhang et al. 2001). This analysis provides dynamically and thermodynamically consistent data in terms of the column budgets of mass, heat, moisture and momentum (Table 6), with minimal adjustments in the observed soundings. Details of the ARM IOP observations can be found in Ghan et al. (2000). A detailed description of the synoptic conditions for this case is provided by Xie et al. (2001).

The large-scale advective cooling rates associated with the major precipitation event of Subcase A reach 1.8 K h^{-1} at 7 km on Julian Day 181 (Fig. 2a), while the large-scale advective moistening rates have maxima of 0.4 g kg^{-1} h^{-1} at 2 km and 5 km, respectively (Fig. 2b). The zonal wind component has a weak deep shear for most of the subperiod except for moderate low-level shear in the last 36 h that is associated with the major precipitation event (Fig. 2c). In Subcase B, the large-scale advective cooling maxima (0.5, 0.3 and 0.4 K h^{-1}, respectively) coincide with the observed surface precipitation maxima rather well (Fig. 1) and so do the large-scale

---

6. Observations of surface precipitation rates were combined from the rain gauges at the central facility, four boundary layer facilities and the Oklahoma and Kansas Mesonet stations, as well as radar retrievals.
7. The observational data set used in this intercomparison study can be obtained from the ARM Archives Data via the ARM webpage at http://www.arm.gov/.

advective moistening maxima (0.1 - 0.4 g kg^{-1} h^{-1}). However, an advective drying maximum (0.2 g kg^{-1} h^{-1}) appears between 2 km and 5 km during this precipitation event, which might not be favorable for the initiation of cumulus convection. The zonal wind component also shows weak deep shear for most of the subperiod (Fig. 2c).

In Subcase C, the large-scale advective cooling maxima (0.5 K h^{-1}) correspond to the two relatively strong precipitation events reasonably well, and so does the last advective moistening maximum (0.3 g kg^{-1} h^{-1}). The first advective moistening maximum (0.5 g kg^{-1} h^{-1}) occurs before the precipitation event. The precipitation events are preceded by pronounced advective drying maxima. The first drying maximum (-0.5 g kg^{-1} h^{-1}) is probably an artifact of the missing soundings on Julian Day 195. The zonal wind shear is rather weak for this subperiod (Fig. 2c).

The subperiod-mean column advective moistening rates of Subcases B and C are small, compared to the precipitation rates (Table 6), because of the presence of large advective dryings during these two subperiods (Fig. 2b). Although the subperiod-mean surface evaporation is a major contribution to the moisture budget, precipitation processes are more tightly related to the large-scale advective cooling and the heat storage (Table 6). This is fundamentally different from that of tropical convection, where the heat storage is negligible and both large-scale advective cooling and moistening rates are closely related to precipitation processes.

4. Results

Two major types of the intercomparison results are shown in this paper: the subperiod-mean profiles and time series of surface or vertically integrated variables. Most of the variables shown in this section will be compared with available observations, except for cloud mass fluxes and condensate mixing ratios, for which no data is available. All of them are temporally and spatially averaged, i.e., 3 h or the entire subperiod in time, and the entire horizontal domain in space.

a. Column heat and moisture budgets

The subperiod-mean surface precipitation rates, heat and moisture storages and imbalances are shown for all three subcases in Table 8. The heat and moisture storages are calculated from the differences between the 3-hourly averaged profiles at the end of each simulation and the observed initial profiles of each subcase. Use of Table 6 allows us to calculate the probable budget imbalances in the models by assuming that the prescribed large-scale advective forcings, radiative heating and surface turbulent fluxes are identical to the observed in all CRMs [see (1) and (2)]. Table 8 shows that the heat and moisture imbalances for most CRMs are within ± 20 W m^{-2}, which is equivalent to 0.7 mm day^{-1} of surface precipitation rate. This is within uncertainties of measurements such as radiative fluxes at the surface and the top of the atmosphere. The lack of perfect budget balances[8] is likely related to a combination of: 1) the vertical interpolation of the forcing data with 50 hPa resolution to model vertical levels (Table 3), 2) the sampling frequency of surface precipitation, 3) the vertical interpolation of prescribed radiative heating rates above 115 hPa, and 4) the possibly incorrect initial soundings. Model deficiencies cannot be completely ruled out from the imbalances shown in Table 8.

The subperiod-mean surface precipitation rates show remarkable agreements among the CRMs, that is, within 20% of the observed rates for most CRMs and within 5% for a few CRMs (Tables 8 and 9). The simulated precipitation rates are lower than the observed rates in the GFDL CRM but higher than the observed in the 2D CSULEM for all three subcases. Other interesting features appearing in Table 8 are that 1) the 3-D CRMs generally produce lower precipitation rates (smaller heat storages and larger moisture storages) than their 2-D counterparts, 2) all CRMs except for 2D CSULEM and 2D UKLEM produce lower precipitation rates than the observed in

---

8. In all models, the surface pressure is set to be 968.7 hPa except for GFDL CRM, which follows the observed surface pressure. An additional term is introduced in the budget equations that is related to the change of surface pressure. This term is especially large in Subcase A but not considered in Table 8 for consistency among the CRMs.

Subcase A, and 3) all CRMs except for GFDL CRM produce higher precipitation rates than the observed in Subcase B.

The subperiod-mean heat and moisture storages show large differences among the models; i.e., some models produce much larger (or smaller) storages than the observed that are beyond the uncertainties in the budgets discussed earlier. This suggests that there are some significant differences in cloud-scale dynamics and microphysics among the models. Comparison between the 2-D and 3-D heat and moisture storages suggests that cloud-scale dynamics plays an important role, which is particularly large in CSULEM.

b. Temporal evolution of surface precipitation and precipitable water

Left panels of Fig. 3 show that all CRMs capture the overall temporal evolution of surface precipitation rates in Subcases A and B and most CRMs have difficulties simulating the observed temporal evolution of Subcase C, in terms of amplitudes and durations of precipitation events. The high-frequency variations of surface precipitation rates in all subcases, for example, higher amplitudes and some phase differences from observations, could be also attributed to a single realization of the simulations. An ensemble of simulations with slightly different initial conditions are expected to provide more smoothly varying time series (e.g., Xu and Randall 1996).

Another common feature among the models is that several precipitation events (often the first) are delayed by several hours in some CRMs. The delay is most pronounced in the first precipitation event of Subcase B for all CRMs where the onset of precipitation is about 6 h after the observed precipitation event. As mentioned in section 2b, for this intercomparison and the previous one (Case 2), all models were initialized with horizontally homogeneous soundings apart from small random temperature perturbations applied to the lowest model layers. In the Tropics (Case 2), these perturbations were able to induce convection because of the small inhibition and large source of moisture. In the present case, these small perturbations are not able to readily generate convective circulations due to the large inhibitions at the boundary layer top and the drier

environment. Convection is therefore delayed until large amounts of moisture are built up in the boundary layer (e.g., Julian Day 190 in Fig. 3). This is easily understood from the column moisture budget (2). In the absence of surface precipitation, column moisture has to increase as the large-scale moistening occurs.

There are several potential reasons why the convection is delayed in Case 3 (especially Subcase B) and it is likely that all are important to some extent. Observations suggest that many convective events in the midlatitude are initiated by mesoscale circulations but these are not included in the initialization procedure proposed for this case. It is also likely that the CRMs resolution of the boundary layer is important as they need to generate shallow cumulus before the deep convection (i.e., overcoming the large inhibition). The current choice of 2 km is too low for this. Finally, the presence of large-scale advective drying around 2 km on Julian Day 190.5 is probably another reason for the delay in Subcase B (Fig. 2) because the drying prevents further moistening of the environments for initiating convection. That is, the large-scale destabilization in the middle/upper troposphere alone is not sufficient to initiate convection in Subcase B.

The temporal evolution of precipitable water, which measures the total water vapor mass in a vertical column, is examined next (right panels of Fig. 3). The general characteristics of the observed temporal evolution of precipitable water[9] are captured by all CRMs. The intermodel differences are small at the beginning of each subperiod before precipitation occurs, as expected from (2), but increase as the model integration time increases because there are intermodel differences in the intensity and initiation time of precipitation events. For example, the temporal evolution is rather similar among the models for the first two days of Subcase C except for EULAG, but it diversifies greatly in the last two and a half days, due to the large intermodel differences in surface precipitation rates. This is likely resulted from the interaction between cloud-scale dynamics and microphysics. Some errors in the specification of large-scale forcings in EULAG for this sub-

9. The observations are based upon radiosonde and microwave radiometer (MWR) measurements (Liljegren 1994).

13

case cannot be ruled out. Subcase A shows the same behavior more dramatically; i.e., an inter-model difference of 9 kg m^{-2} after the major precipitation event (Fig. 3). A most likely cause for this is that representations of evaporation, sublimation and melting processes are inadequate for midlatitude convection in some cloud microphysics schemes.

Other noticeable features in the right panels of Fig. 3 are differences in the impact of the delayed initiation of convection on the temporal evolution of precipitable water among the CRMs and some significant differences between the 2-D and 3-D results (Table 9). Precipitable water is much larger at the end of 3-D simulations than for their 2-D counterparts. This is resulted proba-bly from the accumulative effects of the differences in cloud-scale circulations between 2-D and 3-D models and possibly smaller domain sizes in 3-D simulations, which impact cloud micro-physical processes and their interactions with the environment. Larger cloudy areas (shown in sec-tion 4e) but less intense precipitation in 3-D simulations are associated with the more humid environments (Table 9).

c. Temperature and moisture profiles

First of all, let us examine the impact of the delayed occurrence of the first precipitation event of each subperiod on the temperature and water vapor mixing ratio departures from observa-tions. In Subcase B, the observed maximum precipitation occurs at 30 h, while the simulated max-ima appear between 33 and 38 h (Fig. 3). Between 30 and 36 h (early stages of simulated precipitation events), temperature and moisture departures are determined by the large-scale advective effects (Figs. 2a and 2b). The lapse rates are more unstable and moisture increases in the lower/middle tropospheres except for between 1 and 2 km (Fig. 4), because of the imbalance between the large-scale advective forcings and the response of simulated convection.

After the maximum precipitation is reached in the models (39 - 45 h), the atmospheres are significantly more stable and the boundary layer is much drier than the observed in all models, but the middle troposphere is as moist as in the 30 - 36 h period for all models except for GCE

(Fig. 4). The magnitudes of temperature biases are as high as 5 K in Subcase B (3 K in Subcase A and 5 K in Subcase C) before the precipitation event is simulated, but they are about half of the magnitudes after the precipitation event. These magnitudes are directly related to those of large-scale advective cooling before convection initiation (Fig. 2a). Large moisture biases in the lower troposphere correspond to larger temperature biases in the middle troposphere, but with opposite signs, in all subcases before the first precipitation events are simulated. Although the differences in timing of convection initiation are small, the resulting biases are large among the models (Fig. 4). Finally, the temperature and moisture biases are generally small when precipitation events are promptly simulated (not shown).

The all-subcase mean errors of temperature and water vapor mixing ratio are shown in Fig. 5. Common systematic temperature errors occur above 12 km (+ 2 K) and below 3 km (-1 K). The former is probably related to prescribed radiative heating profiles and/or errors in large-scale advective forcing; the latter is probably associated with strong downdrafts (see section 4f). The moisture biases are less than 0.5 g kg^{-1} for most models except for EULAG, GCE and LaRC CRMs. These errors or those of individual subcases (not shown) are smaller than those in Case 2 (Krueger et al. 2001) and about one third of the errors from SCM simulations (Xie et al. 2001).

The root-mean-square (RMS) errors of CRM simulations relative to observations are shown next. Figure 6 shows that the typical magnitudes of RMS temperature departures from observations are 1 - 2 K for Subcase A, and 1 - 3 K for Subcases B and C, with largest departures in the upper troposphere. These are rather close to the range of observed variabilities as measured by the standard deviation of each subperiod (0.5 - 2.5 K) in these subcases. There are secondary maxima of RMS departures around 7 km and in the planetary boundary layer (PBL). The observed PBL depths exhibit diurnal variations between 0.2 and 2.1 km for these subcases (Krueger et al. 2000). Heights of these maximum RMS departures are generally coincident with the large biases caused by the delayed occurrence of the first precipitation event in each subcase

(Fig. 4). If the first precipitation event were adequately simulated, the typical magnitudes of the RMS departures would probably be halved.

Other features appearing in Fig. 6 are that small RMS errors in one subcase does not guarantee small errors in other subcases for a given CRM and there are larger intermodel differences in the PBL and above 11 km. These differences may be chiefly related to those of the systematic biases (Fig. 5a) and possibly the different treatments of gravity wave reflections from the upper boundary of the models.

In addition, a comparison between 2-D and 3-D simulations from CSULEM and UKLEM shows that the results are similar (Figs. 5 and 6). Little improvement is shown with 3-D simulations due to the small domains used, which is also mostly true for the results shown in the rest of the paper. This finding, in agreement with Grabowski et al. (1998), justifies the usage of 2-D models to examine statistical properties of convection, at least, the mean fields presented in this study.

The RMS errors of water vapor mixing ratio are larger in the lower troposphere, i.e., greater than 1 g kg^{-1} in the PBL where the mixing ratio is also larger (Fig. 7), compared to the observed variabilities of up to 1.2 g kg^{-1}, as measured by the standard deviation of each subperiod. The largest RMS errors occur in Subcases B and C, probably related to more significantly delayed initiation of convection. The large moisture errors in the PBL are caused by the delayed occurrence of the first precipitation event (Fig. 4), and due perhaps to deficiencies of turbulence parameterizations. The latter is partially indicated by the large differences in the PBL moisture biases among the models. In addition, it is difficult to point out which models perform better, based upon the results shown in Fig. 7 although EULAG, GCE and LaRC (in particular, Subcase B) CRMs have relatively larger errors that are mostly related to the systematic biases (Fig. 5b). Nevertheless, these results suggest that the observed moisture variations are more difficult to simulate.

When compared to the Case 2 study of tropical convection, the departures from the observations for all three subcases are comparable. The data quality of Case 2 is perhaps not as high as

that of the present case. However, the delayed occurrence of the first precipitation event is largely responsible for the large departures shown in Figs. 6 and 7. Therefore, the performance of CRMs is reasonably acceptable for simulating midlatitude continental convection, relative to that of tropical oceanic convection (Krueger et al. 2001; Xu and Randall 2000a). Moreover, prompter initiation of the first precipitation events in all subcases should significantly reduce the temperature and moisture departures from observations (Fig. 4). Finally, despite the noticed shortcomings of these CRM simulations, shortcomings at least partly explained by oversimplifications in the initiation procedure, the temperature and water vapor mixing ratio simulated by CRMs are much better than those from SCMs (Ghan et al. 2000; Xie et al. 2001). The intermodel differences of the temperature and moisture departures from observations, are much smaller for CRMs, compared to those among the SCMs (Xie et al. 2001), which gives support for the GCSS strategy.

d. Temporal evolution of cloud liquid water path and total cloud amount

A novel aspect of this intercomparison study is that the ARM Cloud Properties Working Group provides observations of several cloud properties such as the total cloud amount, the cloud liquid water path (CLWP), and the hydrometeor fraction profile, which can be extensively used for intercomparison among CRMs for the first time and provide constraints for the simulated cloud properties.

The CLWPs are measured with MWRs at the central and four boundary facilities of the ARM SGP CART site (Liljegren 1994). The uncertainty of the measurements is ~0.03 kg m^{-2} when raindrops do not contaminate the instrument. Some corrections are also made to eliminate the contamination by raindrops on the instrument. A significant impact of this procedure is that the CLWPs could be severely underestimated during intense precipitation events, for example, on Julian Day 181 of Subcase A (Fig. 8). Also, these "point" measurements might not be fully representative of the domain mean values. Given these shortcomings, left panels of Fig. 8 clearly show that most CRMs produce the CLWP magnitudes comparable to the observed (Table 9).

17

However, all models have difficulties matching the observed temporal evolution. Possible reasons are 1) the delayed occurrence of first precipitation events (no condensate in the first one/ two days), 2) the lack of horizontal advection of hydrometeor (e.g., all models fail to reproduce the maximum on Julian Day 180), 3) "point" measurement vs. domain-mean comparison, and 4) deficiencies in cloud microphysics parameterizations. The temporal evolution of CLWP, as in precipitable water (Fig. 3), in Subcase C of EULAG are rather different from observations and probably caused by either incorrectly imposed large-scale forcings or simplicity of EULAG's microphysical parameterization. The amplitudes of CLWPs in GFDL (GCE) CRM are also greater (smaller) than other models. These intermodel differences are also large in cloud ice water paths (CIWPs; Table 9). Nevertheless, problems in an individual microphysics representation cannot be pinpointed due to uncertainties in the measurements of CLWPs or the lack of measurements in CIWPs. Furthermore, the intermodel differences in the magnitudes of moisture departures from observations among the CRMs (Fig. 7) may also contribute to those in CLWPs.

Two observed column cloud fractions are shown in the right panels of Fig. 8, one from satellite observations (GOES-7 satellite; Minnis et al. 1995) and the other from the retrievals of (single) point measurements of ground-based millimeter-wave cloud radar (MMCR; Moran et al. 1998) at the CART central facility. The latter is just a frequency of retrieved cloudy columns that are sampled at 3-min interval. The definition of a cloudy column is based upon MMCR reflectivity. The satellite procedure uses a threshold method on the brightness temperature. In general, the MMCR cloud fraction is higher than that given by satellite and there are larger temporal variations in the MMCR cloud fractions when satellite observed cloud fractions are low, due to incoherent spatial and temporal scales of these data. This comparison suggests that uncertainties of column cloud fraction observations are in the range of 10 - 30%.

The column cloud fractions show some temporal correlations between models and observations, even though the intermodel differences are probably greater than those in CLWP (Fig. 8).

The simulated column cloud fractions are calculated, based upon the grid-column cloud liquid water + ice path exceeding a threshold of 0.01 kg m^{-2} (Cahalan et al. 1995; Harshvardhan et al. 1994). This threshold could be too high to include many MMCR-observed thin cirrus clouds (Mace et al. 2001). It should also be noted that these clouds are probably not fully resolved by models, with vertical spacings of 500 - 1000 m (Table 3). Therefore, the magnitudes of observed and simulated column cloud fractions are expected to differ significantly (see Table 9).

After the first day (Subcases A and B) or the first two days (Subcase C), most CRMs produce temporal evolution of column cloud fractions somewhat similar to the observations. CNRM, GFDL, LaRC and UKLEM reach the observed overcast conditions on a few occasions. However, the column cloud fractions produced by most models are smaller than the observations, especially by CSULEM, GCE and UCLA/CSU (right panels of Fig. 8). This is mainly due to the lack of the low-level clouds, according to a comparison between satellite-observed and simulated cloud amounts for different layers (Xu and Randall 2000a). The lack of subgrid saturation parameterizations in most CRMs may be one of the reasons for this discrepancy, because 1- or 2-km grid size is too coarse to resolve many small clouds, especially in the lower troposphere. Finally, it is interesting to notice that the cloud fractions are generally higher from 3-D models, due to 3-D cloud dynamics, which allows convection-induced subsidence to spread over the third dimension.

Another common feature among the CRMs is the delayed development of clouds in the first day of each subcase (Fig. 8). The lack of the agreement in the temporal variations after the first day of each subcase is most likely related to the lack of horizontal hydrometeor advection in the upper troposphere (Petch and Dudhia 1998).

e. Cloud property profiles

For all cloud property and mass flux profiles shown hereafter, the mean profiles averaged over all three subcases are produced, instead of those of an individual subcase. The latter were shown in Xu et al. (2000). This procedure does not impact the discussion of the results.

Figure 9 shows the mean profiles of mixing ratios of cloud water, cloud ice, rainwater, snow, graupel/hail, and their sum (total hydrometeor mixing ratio). There are no observations available that can be used to compare with model results. Intermodel differences in cloud water mixing ratios are smaller than those in cloud ice mixing ratios. As far as the profiles of cloud water mixing ratios are concerned (Fig. 9a), all models agree with each other well except for EULAG which features an extremely simple microphysics parameterization. Among the models with 5-category microphysics, the heights of maximum cloud water mixing ratios are generally similar and the magnitudes are only slightly different (smallest by GCE and largest by LaRC). This result is expected due to their similar representations of warm-phase cloud microphysics, i.e., some variations of the Kessler (1969) scheme.

The intermodel differences in the magnitudes of cloud ice mixing ratios are significant (Fig. 9b). The heights of the maximum values are also different (7.5 km in GFDL to 10 km in 3-D CSULEM, GCE and UKLEM). For example, UKLEM shows the smallest values in the middle troposphere, GFDL has its maximum at 7.5 km and LaRC has the smallest maximum value. Surprisingly, the cloud ice mixing ratio profile of EULAG is rather similar to the other models with the Lin et al./Rutledge and Hobbs ice microphysics schemes, although profiles of other water species are not. The additional dimension significantly impacts the cloud ice/snow mixing ratios, lifting the profiles upwards (CSULEM) or increasing the magnitudes (UKLEM, not shown), which suggests that cloud-scale dynamics are different between 2-D and 3-D simulations.

The sum of cloud water and cloud ice mixing ratios (Fig. 10a) reveals the same intermodel differences as shown in Figs. 9a and b. These differences are, however, very small, compared to the simulations of the same case by SCMs (Fig. 10b; Xie et al. 2001). None of the SCMs can capture the magnitudes and the ensemble vertical profiles produced by the CRMs. The ensemble profiles of hydrometeor mixing ratios from CRMs are probably trustworthy as a surrogate to observations.

The total hydrometeor mixing ratio does not depend upon the details of conversion processes among water/ice species, but does depend upon their conversions with water vapor and the vertical transport of the hydrometeors both through the in-cloud dynamics and gravitational fall out of the hydrometeors. Apparently, there is consistency for the profiles of total hydrometeor mixing ratios among the CRMs except for EULAG and for the middle troposphere (Fig. 9c). GCE and LaRC CRMs have hail, instead of graupel, as one of the ice-phase categories, for simulating midlatitude convection. Both have smaller total hydrometeor mixing ratios between 3 and 9 km than the other models. EULAG show appreciably large differences in the middle/upper troposphere from other models mainly because snow mixing ratios are much larger than other models (Fig. 9e), which are needed to account for the same precipitation flux due to the smaller snow terminal velocity than the missing hail/graupel species (Table 4). The large rainwater amount in EULAG and GFDL (Fig. 9d) is due perhaps to the omission of graupel/hail as one of the ice-phase categories. The large rainwater mixing ratio near the surface for GFDL CRM seems to be inconsistent with the smallest subperiod-mean precipitation rates (Tables 8 and 9).

Another feature of Fig. 9c is that there are larger intermodel differences in the middle/upper troposphere, compared to cloud water or cloud ice mixing ratio (Figs. 9a and b). Among the precipitating species, rainwater mixing ratio profiles are mostly similar among the models except for CNRM, EULAG and GFDL (Fig. 9d). Those of snow and graupel/hail are less similar (Figs. 9e and f). Perhaps it is worth pointing out that there is no reason to believe there would be "rain" throughout the troposphere. The freezing of rain is probably the main process missing in the 4-category microphysics parameterizations. Also, the small cloud ice and graupel mixing ratios in the middle troposphere of UKLEM are partially compensated by the large snow mixing ratios there. These intermodel differences could partly be due to the difficulties of ice-phase microphysics representations in CRMs. However, the definitions of what exactly is meant by ice,

snow and graupel may differ from model to model which makes a direct comparison of individual species difficult.

Next, observed hydrometeor fractions are compared with CRM results (Fig. 11). They are based upon the retrievals of MMCR measurements that are averaged on 3-min interval. Whether or not clouds are detected at a height by the MMCR at the central facility of ARM SGP CART site is dependent upon a height-dependent reflectivity threshold (-60 to -45 dBZ; Clothiaux et al. 1999). The reflectivity is contributed not only by cloud water droplets and ice particles, but also by precipitating hydrometeors. The MMCR measured frequency is thus called "hydrometeor fraction." Similarly, the simulated hydrometeor fraction is composed of cloud occurrence and precipitating fractions.

Cloud occurrence from CRMs is defined as the sum of the "cloudy" grid points at a height, divided by the total number of grid points. A CRM grid point is identified as cloudy if the sum of cloud water and cloud ice mixing ratios exceeds 1% of saturation water vapor mixing ratio with respect to liquid (Xu and Krueger 1991). Precipitating fraction from CRMs is similarly defined with a threshold (10^{-6} kg kg^{-1}) on the sum of precipitating water species. Apparently, the criteria used in CRM diagnoses are not identical to those used in the retrievals of MMCR measurements.

The intermodel consistency for cloud occurrences is rather good among the CRMs, especially in the lower and middle troposphere (Fig. 11a). As expected, cloud occurrences are smaller than the MMCR hydrometeor fractions in the lower and middle troposphere but are very comparable to the MMCR estimates in the upper troposphere, especially in GCE and CNRM CRMs.

Most CRMs produce mean profiles of the hydrometeor fractions similar to the observed, although the simulated fractions are higher than the MMCR estimates below 11 km in EULAG, UKLEM, and UCLA/CSU, and for the middle troposphere of GCE, and for the lower troposphere in CNRM, GFDL and LaRC (Fig. 11b). However, both 2-D and 3-D CSULEMs have lower hydrometeor fractions than the MMCR estimates. These intermodel differences in hydrometeor

fractions are mostly related to those of the precipitating water (Fig. 9). The small threshold used in the diagnosis of precipitating fractions is another reason. A diagnosis that is consistent with the MMCR retrievals is needed in order to pinpoint the significance of model biases from the MMCR measurements and to suggest improvement for cloud microphysics representations in CRMs.

f. Cloud mass fluxes

Particularly essential to improve cloud parameterizations are variables such as cloud mass fluxes (M_c). There are no corresponding direct observations available. The updraft, downdraft mass fluxes and their sum (M_c) are compared in this section. Updraft mass flux is defined as:

$$M_u = \int_\sigma (\rho w d\sigma) \qquad \text{if } \{w > 0, \text{cloud}\}, \qquad (3)$$

where $\bar{\rho}$ is the density of air, and σ is the updraft area which satisfies the criterion of cloud occurrence mentioned earlier. Downdraft mass fluxes (M_d) are composed of saturated downdrafts (ds), which satisfy the cloud occurrence criterion, and unsaturated downdrafts (du) with precipitation:

$$M_{ds} = \int_\sigma (\bar{\rho} w d\sigma) \qquad \text{if } \{w < 0, \text{cloud}\}, \qquad (4)$$

$$M_{du} = \int_{\sigma_p} (\bar{\rho} w d\sigma_p) \qquad \text{if } \{w < 0, \text{precipitation}\}, \qquad (5)$$

where σ_p is the precipitation area, which is identified using a larger threshold (10^{-4} kg kg^{-1}) than that used for defining the hydrometeor fraction. Because many different scales of motion are present in CRM simulations, the diagnosed mass fluxes include contributions not only from convective-scale (individual strong drafts), mesoscale circulations (weak stratiform precipitation), but also from gravity waves. Other criteria on defining updrafts and downdrafts have also been used in the literature, mainly using the draft intensity (e.g., Tao et al. 1987; Gray 2000).

The consistency of M_c, which is sum of M_u and M_d, among the models is very good for the mean profiles, as indicated by the small differences from the consensus of all models (thick black

dashed line in Fig. 12a). For comparison, the observed large-scale mass flux, $\overline{M}$ ($\overline{\rho}\overline{w}$, where $\overline{w}$ is the large-scale vertical velocity), is also shown. Most CRMs produce compensating subsidence in the environment of the middle and upper troposphere, i.e., M_c is greater than $\overline{M}$, except for UKLEM and the middle troposphere of CNRM and UCLA/CSU (Fig. 12a). That is, downdrafts are relatively strong in these three models (Fig. 12c).

Another consistent feature among the models is the lack of compensating subsidence in the lower troposphere and the negative M_c in the PBL of all models. The consensus shows the zero-subsidence level at approximately 5 km. This feature is due to the presence of strong precipitating (unsaturated) downdrafts and to the high cloudbase heights (very small M_u below 1 km). The presence of large-scale horizontal advective heating and drying in the lower troposphere (Fig. 2) may favor strong downdraft activity in model simulations so that the compensating subsidence is not produced. A detailed analysis of the downdrafts from CRM simulations is required in order to understand this feature and to improve cumulus parameterizations in GCMs.

The mean profiles of M_u and M_d are also quite consistent among the CRMs (Figs. 12b and 12c). Apparently, their intermodel differences are greater than those of M_c (Fig. 12a) because they respond more directly to the differences in cloud microphysics representations. The intermodel differences in M_u (Fig. 12b) are consistent with those in cloud water mixing ratios (Fig. 9a) and cloud ice mixing ratios (Fig. 9b), except for the large M_u in the upper troposphere of CNRM and UCLA/CSU (perhaps contributed by gravity waves). For example, CNRM and GFDL have the largest cloud water mixing ratios (Fig. 9a) and the largest M_u in the lower troposphere. The smallest cloud ice water mixing ratios correspond to the smallest M_u in the upper tropospheres of EULAG and GFDL (Fig. 9b).

Beyond these intermodel differences, there is a strong consensus among CRMs towards comparable magnitudes in M_u and M_d at most heights. As a result, M_c appears as a relatively small residual of these two mass fluxes (Fig. 12). This feature does not appear in the simulations of tropical oceanic convection (e.g., Xu and Randall 2000a) and may be characteristic of midlatitude convection over land. A change of thresholds used for diagnosis of updraft and downdraft areas is unlikely to impact this result. Clearly, this result stresses the equally important roles of updrafts and downdrafts in midlatitude convection over land. It is probably essential that cloud-related parameterizations capture this feature for a proper representation of these convective systems (Xie et al. 2001).

Further analyses from contributing groups are need to isolate contributions from convective and mesoscale processes, as well as from gravity waves, especially in the upper troposphere. Partitioning of convective and mesoscale processes (Tao and Simpson 1989; Xu 1995) is a well suited approach to understand the physical processes leading to these mass flux profiles.

g. Discussion

The agreements between simulations and observations are rather remarkable in many aspects of the Case 3 simulations, for example, intensity of convective events and timing of some events, and temperature and specific humidity evolution. Some noticeable disagreements are, however, present among the CRMs. Chiefly, the initial convective precipitation events in the CRM simulations of all subcases tend to be delayed relative to observations (Fig. 3). Probable causes for this are 1) the coarse horizontal resolutions (1-3 km), 2) the lack of initial mesoscale circulations due to initialization from horizontally homogeneous soundings, and 3) the initial uniform surface fluxes. Most of these causes are related to oversimplifications in the initiation procedure, not to shortcomings in the models. The delayed occurrence of the initial precipitation events leads to significant departures of simulated thermodynamic profiles from observations (Figs. 6 and 7), which also impact the simulations of cloud fields and cloud properties in the first one to two days.

In the present study, a variety of observations of cloud properties such as cloud liquid water path, column cloud fraction and hydrometeor fraction are available for comparisons with model simulations (Figs. 8 and 11). In general, there are broad agreements with observations for all CRMs, especially in the subperiod-averaged intensities and magnitudes. Some intermodel differences in cloud microphysics parameterizations are readily revealed. It is, however, difficult to pinpoint the causes of the differences between simulations and observations because of large uncertainties in observations, i.e., point measurements vs. areal averages, and in the best-suited definitions of cloud boundaries (lateral, top and bottom) used in the CRM diagnoses. The definitions of cloud boundaries in the CRM diagnoses are not consistent with those of cloud property measurements. For example, the column cloud fractions are all severely underestimated, compared with either MMCR or satellite observations (Fig. 8; Table 9). The hydrometeor fractions show moderate intermodel differences at all heights (Fig. 11), due perhaps to the small thresholds used in the diagnosis of precipitating fractions.

Updraft and downdraft mass fluxes also show some intermodel differences among the models though much smaller than those from SCMs (Fig. 12; Xie et al. 2001). Methods of diagnosing M_u and M_d need to be refined because of the presence of multiple-scale processes in the models, as in the real atmosphere. The mass flux profiles are not available from observations but are needed for evaluating cumulus parameterizations, in addition to the diagnoses of cumulus transports of heat, moisture and momentum.

To further understand the differences between simulations and observations and the intermodel differences, further analyses of observations are needed, based upon mesonet measurements, gridded satellite and radar precipitation data, to improve the variational analysis of the forcing data, e.g., obtaining the horizontal condensate advection. Furthermore, model sensitivity studies will be helpful to reduce the extent of disagreements between models and observations, for example, sensitivities to horizontal or vertical resolutions, representations of microphysical pro-

cesses, and relaxations of oversimplifications in the initiation and forcing methods. In addition, some differences between 2-D and 3-D results also need to be further analyzed because some 3-D results do not show any superiority of the additional dimension. Sensitivity studies by some contributing groups would help finding out the causes of some intermodel differences and deficiencies found in this study; and addressing some issues raised in this study, especially those related to cloud microphysics representations. Additional sensitivity studies are also needed to allow cloud-radiation interactions and the interactions between clouds and land-surface processes in the simulations of midlatitude convection. These sensitivity studies are beyond the scope of this intercomparison but should provide very useful findings in the future.

5. Conclusions

In summary, this intercomparison study has shown:

- CRMs can reasonably simulate midlatitude continental summer convection observed at the ARM CART site in terms of convective intensity, temperature and specific humidity evolution;

- Delayed occurrences of the initial precipitation events are a common feature for all three subcases among the CRMs, especially Subcase B;

- Observed cloud properties are extensively used to identify some model deficiencies in representations of cloud microphysical processes;

- The 2-D results are very close to those produced by 3-D version of the same models; some differences between 2-D and 3-D simulations are noticed and due likely to the limited domain size and the differences between 2-D and 3-D dynamics;

- Cloud mass fluxes, condensate mixing ratios and hydrometeor fractions produced by all CRMs are similar. Some intermodel differences in cloud properties are likely to be related to those in the parameterizations of microphysical processes;

- The magnitudes of the updraft and downdraft mass fluxes are more comparable in magnitudes than those produced by simulations of tropical oceanic deep convection.

References

Bechtold, P., J. L Redelsperger, I. Beau, M. Blackburm, S. Brinkop, J.-Y. Grandpeix, A. Grant, D. Gregory, F. Guichard, C. Holf, and E. Ioannidou, 2000: A GCSS model intercomparison for a tropical squall line observed during TOGA-COARE. Part II: Intercomparison of single-column models with a cloud-resolving model. *Quart. J. Roy. Meteor. Soc.*, **126**, 865-888.

Boyle, J. D., D. R. Durran, C. Chen, B. A. Colle, M. Georgelin, V. Grubisic, W. R. Hsu, C. Y. Huang, D. Landau, Y. L. Lin, G. S. Poulos, W. Y. Sun, D. B. Weber, M. G. Wurtele, and M. Xue, 2000: An intercomparison of model-predicted wave breaking for the 11 January 1972 Boulder windstorm. *Mon. Wea. Rev.*, **128**, 901-914.

Brown, A. R., S. H. Derbyshire, and P. J. Mason, 1994: Large-eddy simulation of stable atmospheric boundary layers with a revised stochastic subgrid model. *Q. J. Roy. Met. Soc.*, **120**, 1485-1512.

Browning, K. A., 1994: GEWEX cloud system study (GCSS) science plan. *IGPO Publication Series*, **No. 11**, International GEWEX Project Office, 84 p.

Cahalan, R. F., D. Silberstein, and J. B. Snider, 1995: A validation of a satellite cloud retrieval during ASTEX. *J. Atmos. Sci.*, **52**, 3002-3012.

Caniaux, G., J.-L. Redelsperger, and J.-P. Lafore, 1994: A numerical study of the stratiform region of a fast-moving squall line. Part I: General description, and water and heat budgets. *J. Atmos. Sci.*, **51**, 2046-2071.

Cess. R. D., and coauthors: 1989: Interpretation of cloud-climate feedback as produced by 14 atmospheric general circulation models. *Science*, **245**, 513-516.

Clothiaux, E. E., K. P. Moran, B. E. Martner, T. P. Ackerman, G. G. Mace, T. Uttal, J. H. Mather, K. B. Widener, M. A. Miller, and D. J. Rodriguez, 1999: *J. Atmos. & Oceanic Tech.*, **16**, 819-827.

Das, S., D. Johnson, and W.-K. Tao, 1999: Single-column and cloud ensemble model simulations of TOGA COARE convective systems. *J. Meteor. Soc. Japan,* **77,** 803-826.

Deardorff, J. W., 1980: Stratocumulus-capped mixed layers derived from a three-dimensional model. *Bound.-Layer Meteor.*, **18**, 495-527.

Donner, L., C. J. Seman, and R. S. Hemler, 1999: Three-dimensional cloud-system modeling of GATE convection. *J. Atmos. Sci.*, **56**, 1885-1912.

Gates, W. L., 1992: AMIP: The Atmospheric Model Intercomparison Project. *Bull. Amer. Meteor. Soc.*, **73**, 1962-1970.

Ghan, S. J., D. A. Randall, K.-M. Xu, R. Cederwall, D. Cripe, J. Hack, S. Iacobellis, S. Klein, S. K. Krueger, U. Lohmann, J. Pedretti, A. Robock, L. Rotstayn, R. Somerville, G. Stenchikov, Y. Sud, G. Walker, S. C. Xie, J. Yio, and M.-H. Zhang, 2000: An intercomparison of single column model simulations of summertime midlatitude continental convection. *J. Geophys. Res.*, **105**, 2091-2124.

Grabowski, W. W., 1998: Toward cloud resolving modeling of large-scale tropical circulations: A simple cloud microphysics parameterization. *J. Atmos. Sci.*, **55**, 3283-3298.

--------, and P. K. Smolarkiewicz, 1996: On two-time-level semi-Lagrangian modeling of precipitating clouds. *Mon. Wea. Rev.*, **124**, 487-497.

--------, X. Wu, and M. W. Moncrieff, 1996: Cloud-resolving modeling of tropical cloud systems during Phase III of the GATE. Part I: Two-dimensional experiments. *J. Atmos. Sci.*, **53**, 3684-3709.

--------, X. Wu, M. W. Moncrieff, and W. D. Hall, 1998: Modeling of cloud systems during Phase III of GATE. Part II: Effects of resolution and the third spatial dimension. *J. Atmos. Sci.*, **55**, 3953-3970.

Gray, M. E. B., 2000: Characteristics of numerically simulated mesoscale convective systems and their application to parameterization. *J. Atmos. Sci.*, **57**, 3264-3282.

Guichard, F., J.-L. Redelsperger, J.-P. Lafore, 2000: Cloud-resolving simulation of convective activity during TOGA-COARE: Sensitivity to external sources of uncertainties. *Q. J. Roy. Meteor. Soc.*, **126**, 3067-3096.

Harshvardhan, B. A. Wielicki, and K. M. Ginger, 1994: The interpretation of remotely sensed cloud properties from a model parameterization perspective. *J. Climate*, **7**, 1987-1998.

Held, I. M., R. S. Hemler, and V. Ramaswamy, 1993: Radiative-convective equilibrium with explicit two-dimensional moist convection. *J. Atmos. Sci.*, **50**, 3909-3927.

Kessler, E., 1969: *On the Distribution and Continuity of Water Substance in Atmospheric Circulation. Meteor. Monogr.,* **32***, Amer. Meteor. Soc.*, 84 pp.

Khairoutdinov, M., and Y. L. Kogan, 1999: A large-eddy simulation model with explicit microphysics: Validation against aircraft observations of a stratocumulus-topped boundary layer. *J. Atmos. Sci.*, **56**, 2115-2131.

Krueger, S. K., 1988: Numerical simulation of tropical cumulus clouds and their interaction with the subcloud layer. *J. Atmos. Sci.*, **45**, 2221-2250.

--------, Q. Fu, K. N. Liou, and H.-N. Chin, 1995: Improvements of an ice-phase microphysics parameterization for use in numerical simulations of tropical convection. *J. Appl. Meteor.,* **34,** 281-287.

--------, S. M. Lazarus, Y. Luo, and K.-M. Xu, 2000: Interactions of deep cumulus convection and the boundary layer over the Southern Great Plains. *14th Symp. on Boundary Layers and Turbulence, Amer. Meteor. Soc.*, Aspen, CO, 114-117.

Krueger, S. K., S. M. Lazarus, P. Bechtold, S. Chen, D. Cripe, L. Donner, W. W. Grabowski, M. Gray, D. Gregory, F. Guichard, H. Jiang, D. Johnson, R. McAnelly, J. C. Petch, D. A. Randall, J.-L. Redelsperger, C. Seman, H. Su, W.-K. Tao, X. Wu, and K.-M. Xu, 2001: Intercomparison of multi-day simulations of convection during TOGA COARE with several cloud-resolving and single-column models. (*In Preparation; may be submitted to QJ*)

Kuettner, J. P., and D. E. Parker, 1976: GATE: Report on the field phase. *Bull. Amer. Meteor. Soc.*, **41**, 11-27.

Liljegren, J. C., 1994: Two-channel microwave radiometer for observations of total column precipitable water vapor and cloud liquid water path. *Proceedings of the Fifth Symposium on Global Change,* Jan. 23-28, 1994, Nashville, TN, *Amer. Meteor. Soc.*, Boston, MA, 266-269.

Lilly, D. K., 1967: The representation of small-scale turbulence in numerical simulation experiments. *Proc. IBM Scientific Computing Symp. on Environmental Science*, Yorktown Heights, NY, 195-210.

Lin, Y.-L., R. D. Farley, and H. D. Orville, 1983: Bulk parameterization of the snow field in a cloud model. *J. Climate Appl. Meteor.,* **22**, 1065-1092.

Lipps, F. B., and R. S. Hemler, 1986: Numerical simulation of deep tropical convection associated with large-scale convergence. *J. Atmos. Sci.*, **43**, 1796-181

Mace, G. G., E. E. Clothiaux, and T. P. Ackerman, 2001: The composite characteristics of cirrus clouds: Bulk properties revealed by one year of continuous cloud radar data. *J. Climate*, **14,** 2185-2203.

Minnis, P., W. L. Smith, Jr., D. P. Garber, J. K. Ayers, and D. R. Doelling, 1995: Cloud properties derived from GOES-7 for Spring 1994 ARM Intensive Observing Period using Version 1.0.0 of ARM satellite data analysis program. *NASA Reference Publication 1366*, NASA Langley Research Center, Hampton, VA 23681-0001.

Moeng, C.-H., W. R. Cotton, C. S. Bretherton, A. Chlond, M. Khairoutdinov, S. K. Krueger, W. S. Lewellen, M. K. MacVean, J. R. M. Pasquier, H. A. Rand, A. P. Siebesma, B. Stevens, and R. I. Sykes, 1996: Simulation of a stratocumulus-topped planetary boundary layer: Intercomparison among different numerical codes. *Bull. Amer. Meteor. Soc.*, **77**, 261-278.

Moncrieff, M. W., S. K. Krueger, D. Gregory, J.-L. Redelsperger, and W.-K. Tao, 1997: GEWEX Cloud System Study (GCSS) Working Group 4: Precipitating convective cloud systems. *Bull. Amer. Meteor. Soc.*, **78**, 831-845.

Moran, K. P., B. E. Martner, M. J. Post, R. A. Kropfli, D. C. Welsh, and K. B. Widener, 1998: An unattended cloud-profiling radar for use in climate research. *Bull. Amer. Meteor. Soc.*, **79**, 443-455.

Petch, J. C., and J. Dudhia, 1998: The importance of the horizontal advection of hydrometeors in a single-column model. *J. Climate*, **11**, 2437-2452.

Randall, D. A., K.-M. Xu, R. C. J. Somerville, and S. Iacobellis, 1996: Single-column models and cloud ensemble models as links between observations and climate models. *J. Climate*, **9**, 1683-1697.

--------, J. Curry, P. Duynkerke, S. K. Krueger, M. W. Moncrieff, B. Ryan, D. O. Starr, M. Miller, W. Rossow, G. Tselioudis, B. A. Wielikci, 2001: The GEWEX cloud system study: A view from 2001. *Bull. Amer. Meteor. Soc.*, (Submitted).

Redelsperger, J.-L., and G. Sommeria, 1986: Three-dimensional simulation of a convective storm: Sensitivity on subgrid parameterization and spatial resolution. *J. Atmos. Sci.*, **43**, 2616-2635.

Redelsperger, J.-L., P. R. A. Brown, F. Guichard, C. Hoff, M. Kawasima, S. Lang, T. Montmerle, K. Nakamura, K. Saito, C. Seman, W.-K. Tao and L. J. Donner, 2000: A GCSS model intercomparison for a tropical squall line observed during TOGA-COARE. I: Cloud-resolving models. *Quart. J. Roy. Met. Soc*, **115,** 823-864.

Rutledge, S. A., and P. V. Hobbs, 1984: The mesoscale and microscale structure and organization of clouds and precipitation in midlatitude cyclones. XII: A diagnostic modeling study of precipitation development in narrow cold-frontal rainbands. *J. Atmos. Sci.*, **41**, 2949-2972.

Schumann, U., 1991: Subgrid length-scales for large-eddy simulation of stratified turbulence. *Theoret. Comput. Fluid Dyn., 2,* 279-290.

Shutts, G. J., and M. E. B. Gray, 1994 A numerical modeling study of the geostrophic adjustment process following deep convection. *Q. J. Roy. Meteor. Soc.*, **120**, 1145-1178.

Smagorinsky, J., 1963: General circulation experiments with the primitive equations. *Mon. Wea. Rev.*, **91**, 99-165.

Smolarkiewicz, P. K., and L. G. Margolin, 1997: On forward-in-time differencing for fluids: An Eulerian/semi-Lagrangian nonhydrostatic model for stratified flows. *Atmos.-Ocean Special*, **35**, 127-152.

Stokes, G. M., and S. E. Schwartz, 1994: The Atmospheric Radiation Measurement (ARM) program: Programmatic background and design of the cloud and radiation test bed. *Bull. Amer. Meteor. Soc.*, **75**, 1202-1221.

Su, H., S. S. Chen, and C. S. Bretherton, 1999: Three-dimensional week-long simulations of TOGA COARE convective systems using the MM5 mesoscale model. *J. Atmos. Sci.*, **56**, 2326-2344.

Swann, H., 1998: Sensitivity to the representation of precipitating ice in CRM simulations of deep convection. *Atmos. Res.*, **48**. 415-435.

Tao, W.-K., and J. Simpson, 1993: The Goddard Cumulus Ensemble Model. Part I: Model description. *Terr. Atmos. Oceanic Sci.*, **4**, 35-72.

--------, --------, 1989: Modeling study of a tropical squall-type convective line. *J. Atmos. Sci.*, **46**, 177-202.

--------, J. Simpson, and S.-T.Soong, 1987: Statistical properties of a cloud ensemble: A numerical study. *J. Atmos. Sci.*, **44**, 3175-3187.

--------, S. Lang, J. Simpson, W. S. Olson, D. Johnson, B. Ferrier, C. Kummerow, and R. Adler, 2001a: Vertical profiles of latent heat release and their retrieval in TOGA COARE convec-

tive systems using a cloud resolving model, SSM/I and radar data. *J. Meteor. Soc. Japan,* **78,** 333-355.

--------, J. Simpson, D. Baker, S. Braun, M.-D. Chou, B. Ferrier, D. Johnson, A. Khain, S. Lang, B. Lynn, C.-L. Shie, D. Starr, C.-H. Sui, Y. Wang and P. Wetzel, 2001b: Microphysics, radiation and surface processes in a non-hydrostatic model. *Meteor. Atmos. Phys.* (accepted).

Webster, P., J., and R. Lukas, 1992: TOGA COARE: The coupled ocean-atmosphere response experiment. *Bull. Amer. Meteor. Soc.*, **73**, 1377-1417.

Wu, X., W. W. Grabowski, and M. W. Moncrieff, 1998: Long-term behavior of cloud systems in TOGA COARE and their interactions with radiative and surface processes. Part I: Two-dimensional modeling study. *J. Atmos. Sci.*, **55**, 2693-2714.

--------, W. D. Hall, W. W. Grabowski, M. W. Moncrieff, W. D. Collins, and J. T. Kiehl, 1999: Long-term behavior of cloud systems in TOGA COARE and their interactions with radia-tive and surface processes. Part II: Effects of ice microphysics on cloud–radiation interac-tion. *J. Atmos. Sci.,* **56,** 3177-3195.

Xie, S. C., R. T. Cederwall, K.-M. Xu, P. Bechtold, D. G. Cripe, A. D. Del Genio, S. J. Ghan, J. J. Hack, S. F. Iacobellis, S. A. Klein, S. K. Krueger, U. Lohmann, J. C. Petch, D. A. Randall, L. D. Rotstayn, R. J. C. Somerville, Y. C. Sud, K. von Salzen, G. K. Walker, A. Wolf, J. J. Yio, G. Zhang, and M.-H. Zhang, 2001: Intercomparison and evaluation of GCM cumulus parameterizations under summertime midlatitude continental conditions. *Q. J. Roy Meteor. Soc.,* (Submitted in May 2001).

Xu, K.-M., 1995: Partitioning mass, heat and moisture budgets of explicitly simulated cumulus ensembles into convective and stratiform components. *J. Atmos. Sci.*, **52**, 551-573.

--------, and S. K. Krueger, 1991: Evaluation of cloudiness parameterizations using a cumulus ensemble model. *Mon. Wea. Rev.*, **119**, 342-367.

--------, D. A. Randall, 1995: Impact of interactive radiative transfer on the macroscopic behavior of cumulus ensembles. Part I: Radiation parameterization and sensitivity test. *J. Atmos. Sci.*, **52**, 785-799.

--------, --------, 1996: Explicit simulation of cumulus ensembles with the GATE Phase III data: Comparison with observations. *J. Atmos. Sci.*, **53**, 3710-3736.

--------, --------, 2000a: Explicit simulation of midlatitude cumulus ensembles: Comparison with ARM data. *J. Atmos. Sci.,* **57**, 2839-2858.

--------, --------, 2000b: Cloud-resolving model simulation of the July 1997 IOP: Comparison with ARM data on short, medium and long subperiod. *Proceedings of the Tenth Atmospheric Radiation Measurement (ARM) Science Team Meeting*, March 13-17, 2000, San Antonio, Texas.

--------, S. K. Krueger, R. T. Cederwall, L. J. Donner, W. W. Grabowski, F. Guichard, D. E. Johnson, M. Khairoutdinov, J. C. Petch, D. A. Randall, C. J. Seman, W.-K. Tao, S. C. Xie, J. J. Yio, and M.-H. Zhang, 2000: Cloud-resolving model intercomparison with the ARM Summer 1997 IOP data. *Proceedings of the Tenth Atmospheric Radiation Measurement (ARM) Science Team Meeting*, March 13-17, 2000, San Antonio, Texas.

Xue, M., K. K. Droegemeier, and V. Wong, 2001: The Advanced Regional Prediction System (ARPS) -- A multi-scale nonhydrostatic atmospheric simulation and prediction tool: Part I: Model dynamics and verification. *Meteor. Atmos. Phy.*, **75**, 161-193.

Zhang, M.-H., and J. L. Lin, 1997: Constrained variational analysis of sounding data based on column-integrated budgets of mass, heat, moisture, and momentum: Approach and application to ARM measurements. *J. Atmos. Sci.*, **54**, 1503-1524.

--------, --------, R. T. Cederwall, J. J. Yio, and S. C. Xie, 2001: Objective analysis of ARM IOP data: Method, feature and sensitivity. *Mon. Wea. Rev.*, **129**, 295-311.

Figure caption

Figure 1: Time series of observed surface precipitation rates during Summer 1997 IOP of the ARM program. The horizontal lines inside the plot show the durations of the three subperiods chosen for this intercomparison study.

Figure 2: Time-height cross sections of (a) observed large-scale advective cooling rates, (b) observed large-scale advective moistening rates, and (c) observed zonal wind components for Subcases A, B and C.

Figure 3: Time series of observed and simulated surface precipitation rates (left panels) and precipitable water (right panels) for Subcases A, B and C. The black solid lines show the observations.

Figure 4: Six-hour averaged temperature and water vapor mixing ratio biases for periods before (30-36 h) and after (39-45 h) the simulated precipitation peaks in Subcase B.

Figure 5: The all-subcase mean errors of temperature and water vapor mixing ratio.

Figure 6: Root-mean-square errors of temperature for Subcases A, B, and C.

Figure 7: Root-mean-square errors of water vapor mixing ratio for Subcases A, B and C.

Figure 8: Time series of observed and simulated cloud liquid water paths (left panels) and the column cloud fraction (right panels) for Subcases A, B and C. The black solid line on the left panels shows the MWR observations. The black solid and dashed lines on the right panels show the observations from MMCR and GOES, respectively.

Figure 9: The all-subcase mean profiles of the mixing ratios of (a) cloud water mixing ratio, (b) cloud ice mixing ratio, (c) total hydrometeor, (d) rainwater, (e) snow and (f) graupel/hail. The black dashed lines in (a), (b) and (c) show the consensus of all models. Unit for all horizontal axes is 0.01 g kg^{-1}. No observations is available for comparison.

Figure 10: Same as Fig. 9 except for the sum of cloud water and cloud ice mixing ratios for (a) CRMs and (b) SCMs. The legends of curves for CRMs are identical to Fig. 9 but those for SCMs are not identified.

Figure 11: Same as Fig. 9 except for cloud occurrence and hydrometeor fractions. Unit for the horizontal axes is percentage.

Figure 12: Same as Fig. 9 except for the net cloud mass flux, updraft and downdraft mass fluxes. The thick black dashed line shows the consensus of all models.

Table 1: Recent CRM/SCM intercomparison studies (the first six papers) and selected CRM studies using observational data sets. A brief description of some major results is listed.

Reference	Large-scale data source	Models	Simulation length	Major results
Redelsperger et al. (2000)	TOGA COARE	8 2-D CRMs, 4 3-D CRMs	7 hours	Broad agreement among CRMs in the overall structure and propagation of the squall line, but less agreement in heating and drying profiles; results sensitive to cloud microphysics and lateral boundary conditions
Bechtold et al. (2000)	TOGA COARE	8 SCMs	7 hours	Good agreement among SCMs in the temporal evolution, but less on thermodynamic structure and convective-stratiform partitioning
Ghan et al. (2000)	July 1995 ARM IOP	11 SCMs, 1 2-D CRM	18 days	Intermodel differences among SCMs larger than uncertainties in prescribing the boundary conditions and the different methods of imposing large-scale forcings
Krueger et al. (2001)	TOGA COARE	8 2-D CRMs, 3 3-D CRMs, 6 SCMs	6 days	Bulk characteristics of convection determined by the large-scale advective tendencies, smaller intermodel differences among CRMs than among the SCMs
This study	Summer 1997 ARM IOP	8 2-D CRMs, 2 3-D CRMs	4 or 5 days	Broad agreement with observations among CRMs in simulating cloud properties for midlatitude continental convection
Xie et al. (2001)	Summer 1997 ARM IOP	15 SCMs	4 or 5 days	Evaluating the performance of different categories of cumulus parameterizations in SCMs and comparison with CRM simulated mass flux profiles
Das et al. (1999)	TOGA COARE	2-D GCE CRM and SCM	7 days	Diurnal variations well simulated by both SCM and CRM, significant differences between SCM and CRM related to those in surface fluxes
Grabowski et al. (1996, 1998)	GATE Phase III	2-D and 3-D NCAR CRM	7 days	Simulating realistic transformations between regimes of GATE convection; 2-D and 3-D realizations of cloud systems compared favorably with GATE observations
Guichard et al. (2000)	TOGA COARE	2-D CNRM CRM	7 days	Uncertainties in large-scale advective forcings impact the relevance of model validation by contrasting various observational datasets with simulation
Su et al. (1999)	TOGA COARE	3-D NCAR MM5	8 days	Reproducing much of the observed temporal variability of thermodynamic profiles with different grid sizes and with/without parameterized cumulus convection
Tao et al. (2001a)	TOGA COARE	2-D GCE CRM	7 days	Inconsistency in the large-scale advective forcings in temperature and water vapor produced large biases
Wu et al. (1998, 1999)	TOGA COARE	2-D NCAR CRM	39 days	Long-term realization of cloud and radiative properties over the warm pool, cloud properties sensitive to ice sedimentation
Xu and Randall (1996)	GATE Phase III	2-D UCLA/CSU CRM	18 days	Majority of the simulated results agree with observations very well, including characteristics of cloud systems
Xu and Randall (2000a)	July 1995 ARM IOP	2-D UCLA/CSU CRM	18 days	Larger differences between simulations and observations than those using GATE data, identifying the differences of statistical properties of midlatitude vs. tropical convection

Table 2: Summary of CRMs used in this intercomparison study.

Model	Model full name	Modeler(s)	Reference(s)
CNRM	Centre National de Recherches Meteo-rologiques	Guichard	Redelsperger and Sommeria (1986); Caniaux et al. (1994)
CSULEM	Colorado State University LES/CRM	Khairoutdinov	Khairoutdinov and Kogan (1999)
EULAG	NCAR EUlerian/semi-LAGrangian cloud model	Grabowski	Grabowski and Smolarkiewicz (1996); Smolarkiewicz and Margolin (1997); Grabowski (1998)
GCE	NASA Goddard Cumulus Ensemble model	Tao, Johnson	Tao and Simpson (1993)
GFDL	NOAA Geophysical Fluid Dynamic Laboratory	Donner, Seman	Lipps and Hemler (1986); Held et al. (1993); Donner et al. (1999)
LaRC	NASA Langley Research Center Advanced Regional Prediction System (ARPS)	Wang, Xu	Xue et al. (2001)
UCLA/ CSU	University of California-Los Angeles/Colorado State University	Xu	Krueger (1988); Xu and Randall (1995)
UKLEM	UK Met Office Large-Eddy Model	Petch	Shutts and Gray (1994)

Table 3: Numerics of cloud resolving models used in this intercomparison study. NFT stands for nonoscillatory forward-in-time while A-B for Adams-Bashforth. The asterisk (*) on vertical layer column indicates that vertically uniform layers are used.

Model	Dimension	Domain	Grid spacing	Time differencing	Time step	Momentum advection	Vertical layers
CNRM	2-D	512x20 km^2	2 km	Leapfrog	12 s	2nd-order	48
CSULEM 2D	2-D	512x27 km^2	2 km	A-B 3rd	10 s	2nd-order	64
CSULEM 3D	3-D	250x250x27 km^3	2x2 km^2	A-B 3rd	10 s	2nd-order	64
EULAG	2-D	600x25 km^2	3 km	NFT	15 s	2nd-order	51*
GCE	2-D	512x20 km^2	1 km	Leapfrog/NFT	6 s	4th-order	41
GFDL	2-D	512x20 km^2	2 km	Leapfrog	2 s	2nd-order	84*
LaRC	2-D	512x26 km^2	2 km	Leapfrog	3 s /6 s	4th-order	53
UCLA/CSU	2-D	512x19 km^2	2 km	A-B 2nd	10 s	2nd-order	34
UKLEM 2D	2-D	500x20 km^2	2 km	Leapfrog	variable	2nd-order	60
UKLEM 3D	3-D	250x250x20 km^3	2x2 km^2	Leapfrog	variable	2nd-order	60

Table 4: Bulk cloud microphysics parameterizations of cloud-resolving models used in this intercomparison study.

Model	Predicted cloud microphysics category	Notes	References
CNRM	cloud water, rain, snow, graupel and cloud ice	relaxing the constant slope and intercept parameter assumptions	Caniaux et al. (1994)
CSULEM	total water (vapor, condensate) and precipitating water	partitioning of two predicted categories into six categories (vapor, cloud water, rain, snow, graupel and cloud ice); all-or-nothing moist adjustment for obtaining condensate water	Hydrometeor conversion rates follow Lin et al. (1983) and Rutledge and Hobbs (1984)
EULAG	cloud condensate (liquid, ice) and precipitating water (rain, snow)	classical Kessler; diagnostic partitioning of liquid and solid phases, no graupel	Grabowski (1998)
GCE	cloud water, rain, snow, hail and cloud ice	modified Lin et al. (1983)	Tao and Simpson (1993); Tao et al. (2001b)
GFDL	cloud condensate (liquid, ice), snow/ice and rainwater	diagnostic partitioning of liquid and ice phases, no graupel	Donner et al. (1999)
LaRC	cloud water, rain, snow, hail and cloud ice	an old version of the GCE microphysics	Tao and Simpson (1993)
UCLA/ CSU	cloud water, rain, snow, graupel and cloud ice	modified Lin et al. (1983)	Lin et al. (1983); Krueger et al. (1995)
UKLEM	cloud water, rain, snow, graupel and cloud ice	also predicting the number concentration of cloud ice particles	Swann (1998)

Table 5: Turbulence parameterizations of cloud-resolving models used in this intercomparison study.

Model	Scheme	Specific features	Reference
CNRM	1.5-order closure	eddy diffusion through TKE equation	Deardorff (1980)
CSULEM	1.5-order closure	eddy diffusion through TKE equation	Deardorff (1980)
EULAG	1.5-order closure	eddy diffusion through TKE equation	Schumann (1991)
GCE	1.5-order closure	eddy diffusion through TKE equation	Deardorff (1980); Tao and Simpson (1993)
GFDL	1st-order closure	deformation- and Richardson number-dependent subgrid-scale formulation	Donner et al. (1999)
LaRC	1.5-order closure	eddy diffusion through TKE equation	Xue et al. (2001)
UCLA/CSU	3rd-order closure	also treat in-cloud turbulence	Krueger (1988)
UKLEM	1st-order closure	Smagorinsky-Lilly model, neutral mixing length assumed to be 250 m	Brown et al. (1994)

Table 6: Observed column heat and moisture budget components for Subcases A, B and C. Unit for all budget components is W m^{-2}.

	Subperiod A	Subperiod B	Subperiod C
LP (precipitation)	237.7	120.7	122.0
LE (evaporation)	117.6	111.2	125.1
SH (sensible heat flux)	38.1	29.1	30.1
Q_R (radiative heating)	-61.7	-48.7	-65.6
LS advective heating rate	-112.1	-42.5	-112.2
LS advective moistening rate	148.1	43.0	11.7
Heat storage	101.8	58.5	-25.7
Moisture storage	26.9	33.4	14.5

.

Table 7: Summary of characteristics of subcases for this intercomparison study.

Subcase	Duration	Characteristics of convection
A	2330 UTC 26-30 June 1997 (Julian Day 178 to 182)	A major precipitation event with a maximum precipitation rate of 3.5 mm h^{-1} on Julian Day 181, and weak precipitation events on Julian Day 179.
B	2330 UTC 7-12 July 1997 (Julian Day 189 to 194)	Three moderate precipitation events with maximum precipitation rates of approximately 1.0 mm h^{-1} (Julian Days 190, 191.5 to 193), with a very short (3 - 5 h) break period between the second and third events.
C	2330 UTC 12-17 July 1997 (Julian Day 194 to 199)	A moderate precipitation event (~ 1 mm h^{-1}) on Julian Day 198 and a few weaker ones (< 0.7 mm h^{-1}) in the middle of the subperiod.

Table 8: Comparison of observed precipitation, heat and moisture storages and their imbalances with model simulations for Subcases A, B and C. The imbalances from observations are due to the lower order finite differencing scheme than in Table 6 for calculating the heat and moisture storage terms. Unit is W m^{-2}.

	LP	Heat storage	Moisture storage	Heat imbalance	Moisture imbalance
			Subcase A		
Observation	237.7	104.2	29.1	2.2	1.1
CNRM	235.9	81.0	56.2	-19.2	26.4
CSULEM 2D	277.6	140.1	9.0	-1.8	20.9
CSULEM 3D	197.2	63.8	86.4	15.8	17.9
EULAG	205.3	78.3	70.5	8.7	10.1
GCE	210.6	75.6	50.0	0.7	-5.1
GFDL	179.4	82.0	44.2	38.1	-41.5
LaRC	198.9	54.7	71.4	-8.5	4.6
ULCA/CSU	211.3	92.4	48.8	16.8	-5.6
UKLEM 2D	241.0	83.7	34.8	-21.6	10.1
UKLEM 3D	204.6	36.4	67.0	-32.5	5.9
			Subcase B		
Observation	120.7	54.6	26.3	-4.0	-7.2
CNRM	130.3	45.5	33.7	-22.7	9.8
CSULEM 2D	146.0	81.6	13.6	-2.3	5.4
CSULEM 3D	122.4	61.6	31.1	1.3	-0.7
EULAG	129.1	67.0	39.1	0.0	14.0
GCE	138.2	70.4	5.0	-5.7	-11.0
GFDL	99.9	34.8	25.9	-4.1	-27.6
LaRC	126.8	36.4	17.8	-18.3	-9.6
UCLA/CSU	121.1	48.2	25.2	-10.8	-7.9
UKLEM 2D	123.6	48.6	23.4	-12.9	-7.2
			Subcase C		
Observation	122.0	-27.5	18.5	-1.8	3.7
CNRM	144.8	-26.6	13.0	-23.7	21.0
CSULEM 2D	143.5	2.8	-3.8	7.0	2.9
CSULEM 3D	81.8	-40.0	42.8	25.9	-12.2
EULAG	124.8	-15.0	35.8	7.9	23.8
GCE	134.9	-10.9	-9.4	1.9	10.7
GFDL	93.7	-69.6	29.1	-5.6	14.0
LaRC	103.6	-64.1	28.9	-20.0	-4.3
UCLA/CSU	111.0	-53.4	26.7	-16.7	1.1
UKELM 2D	108.7	-53.0	35.6	-14.6	7.5
UKLEM 3D	110.5	-57.0	39.0	-19.8	12.7

Table 9: Comparison of simulated subperiod-mean (excluding the first day) precipitable water, surface precipitation rate, cloud liquid water path, column cloud fraction with observations.

| Model	Precipitable water (kg m^{-2})	Total precipitation (mm day^{-1})	cloud liquid water path (g m^{-2})	Cloud ice water path (g m^{-2})	Column cloud fraction
Subcase A					
Observations	40.21	10.78	56.25	n/a	0.499
CNRM	41.04	10.23	41.02	20.96	0.275
CSULEM 2D	38.52	12.01	40.57	60.30	0.192
CSULEM 3D	41.23	8.71	30.96	53.06	0.144
EULAG	41.82	9.20	53.07	26.52	0.204
GCE	39.23	9.69	27.95	47.87	0.130
GFDL	40.80	8.29	43.40	25.21	0.241
LaRC	41.95	9.16	49.47	15.06	0.182
UCLA/CSU	39.82	9.73	37.54	33.81	0.175
UKLEM 2D	38.98	11.32	30.95	83.00	0.333
UKLEM 3D	40.56	9.43	25.91	48.86	0.355
Subcase B					
Observations	42.55	5.14	46.92	n/a	0.597
CNRM	43.00	5.63	50.16	22.86	0.520
CSULEM 2D	41.08	6.35	54.58	50.72	0.243
CSULEM 3D	43.10	5.46	46.20	43.82	0.233
EULAG	44.02	5.58	85.28	23.94	0.326
GCE	39.23	5.97	21.66	38.59	0.181
GFDL	43.17	4.36	85.11	28.21	0.383
LaRC	41.86	5.48	73.67	15.58	0.307
UCLA/CSU	42.11	5.23	41.93	29.52	0.222
UKLEM 2D	41.38	5.74	39.32	58.63	0.378
Subcase C					
Observations	38.89	5.24	34.22	n/a	0.616
CNRM	39.43	6.26	37.13	34.66	0.397
CSULEM 2D	37.03	5.82	30.82	57.93	0.215
CSULEM 3D	39.48	3.58	26.89	53.82	0.273
EULAG	42.75	5.39	80.89	31.23	0.327
GCE	37.83	5.83	12.83	54.03	0.306
GFDL	39.90	4.05	47.32	37.69	0.425
LaRC	39.85	4.48	41.36	17.77	0.338
UCLA/CSU	39.19	4.80	26.58	41.04	0.260
UKELM 2D	37.98	5.39	26.65	64.76	0.311
UKELM 3D	39.10	4.69	35.56	34.45	0.340
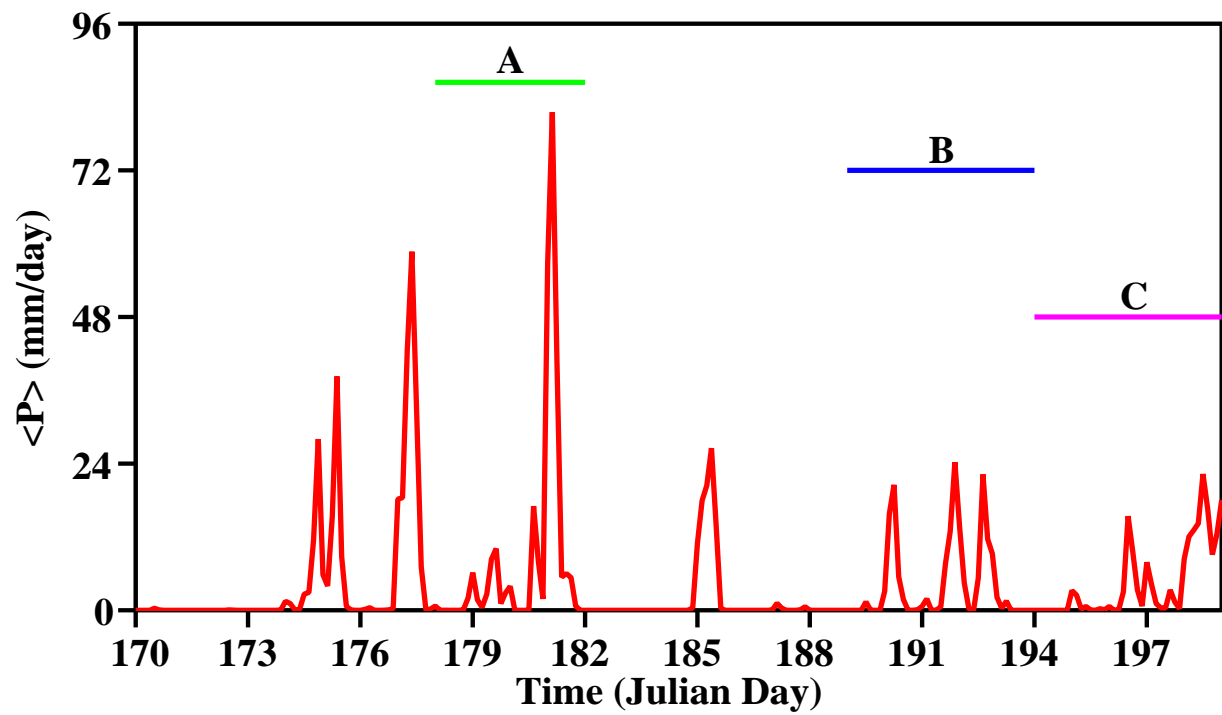
Fig. 1: Time series of observed surface precipitation rates during Summer 1997 IOP of the ARM program. The horizontal lines inside the plot show the durations of the three subperiods chosen for this intercomparison study.
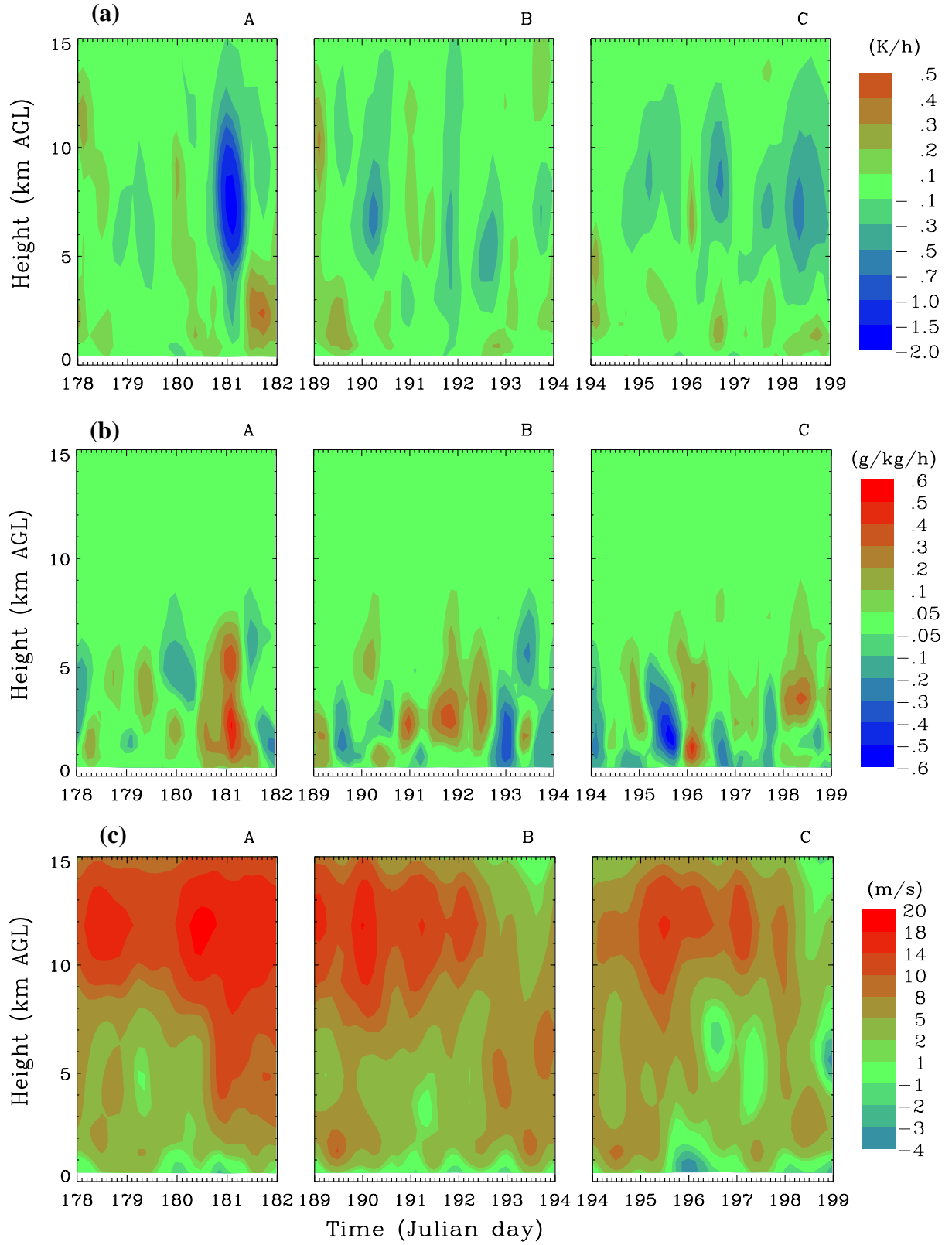
Fig. 2: Time-height cross sections of (a) observed large-scale advective cooling rates, (b) observed large-scale advective moistening rates and (c) observed zonal wind components for Subcases A, B and C.
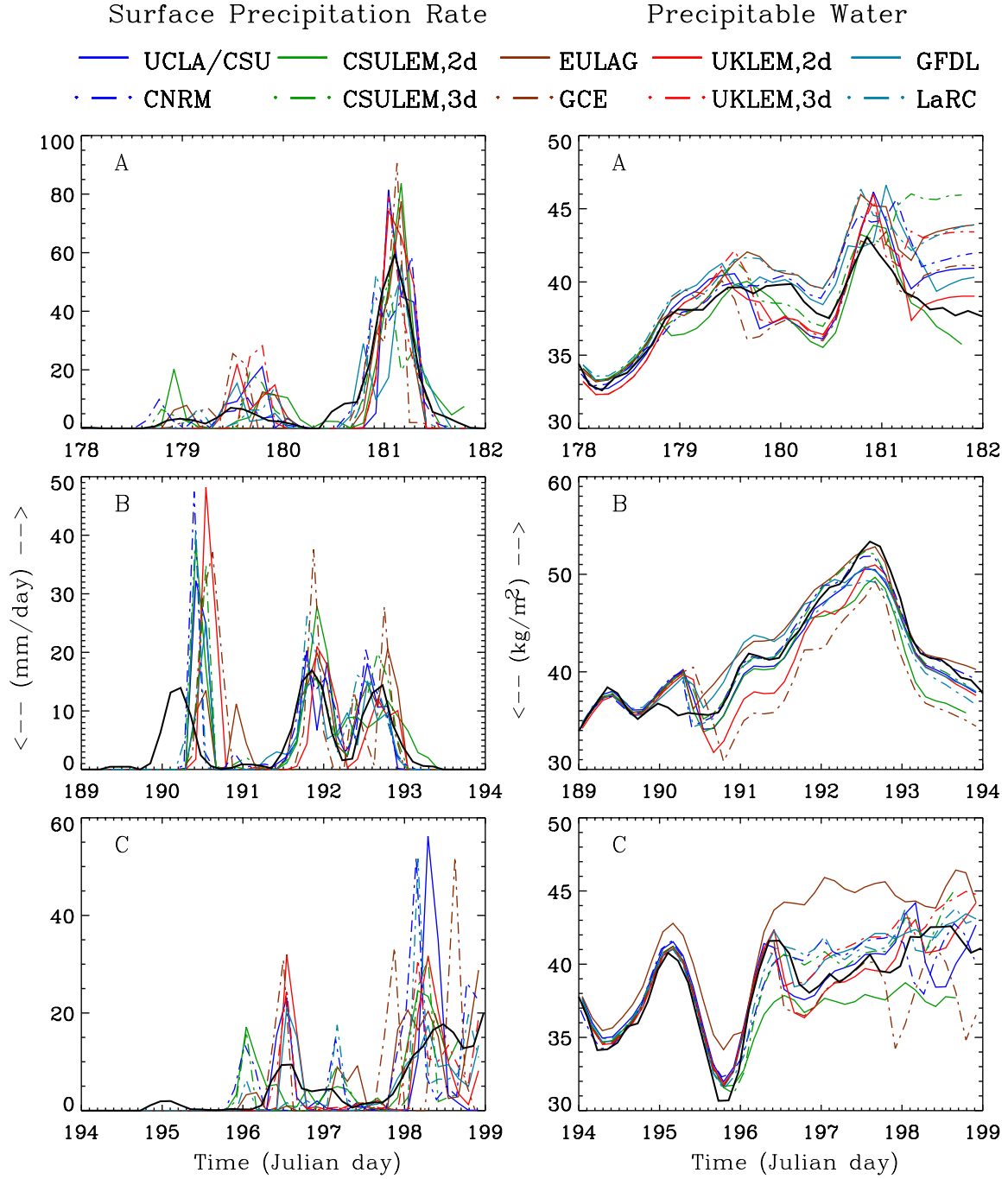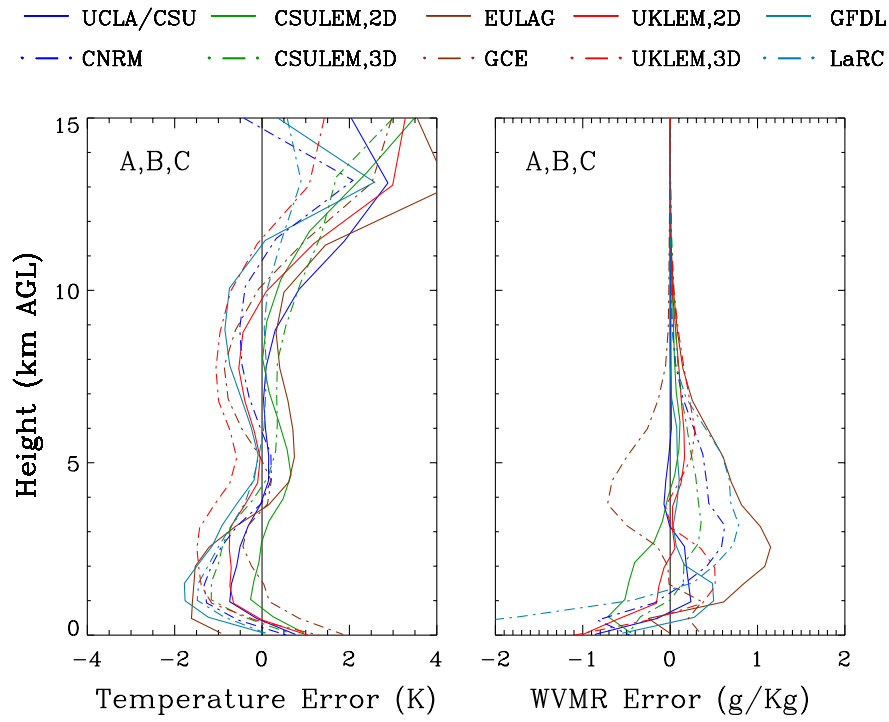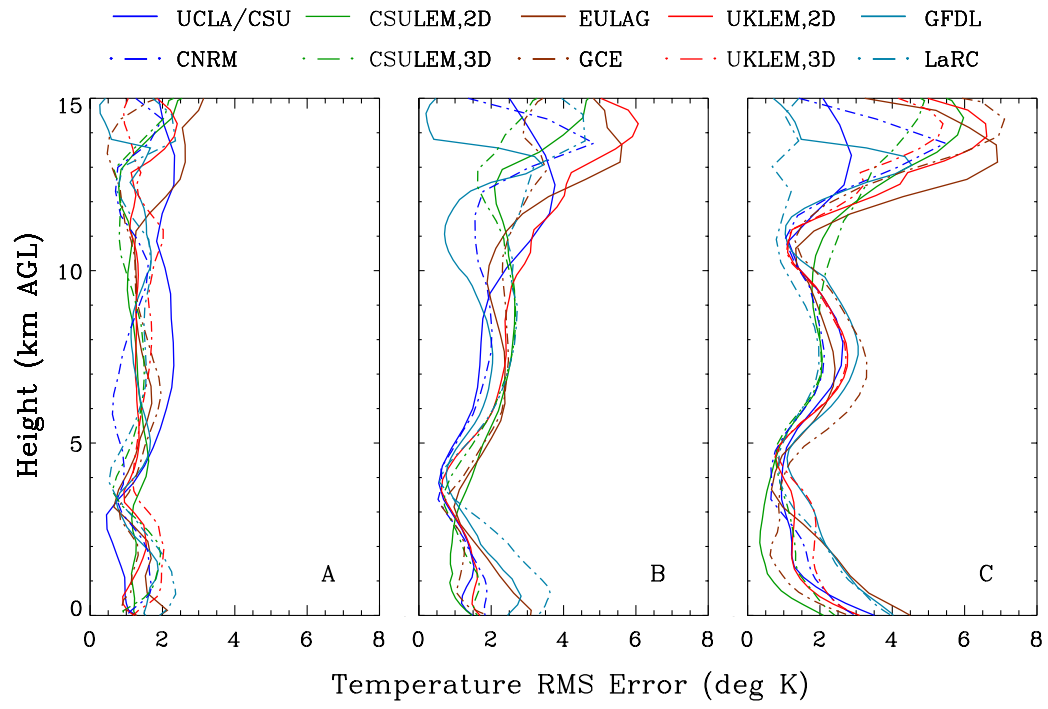
Fig. 3: Time series of observed and simulated surface precipitation rates (left panels) and precipitable water (right panels) for Subcases A, B and C. The black solid lines show the observations.

49
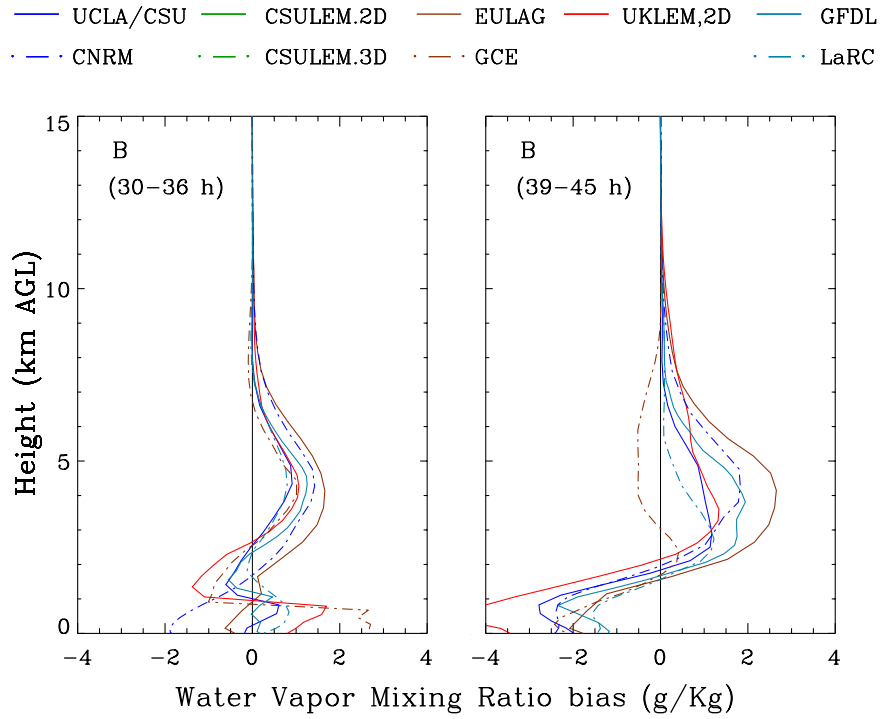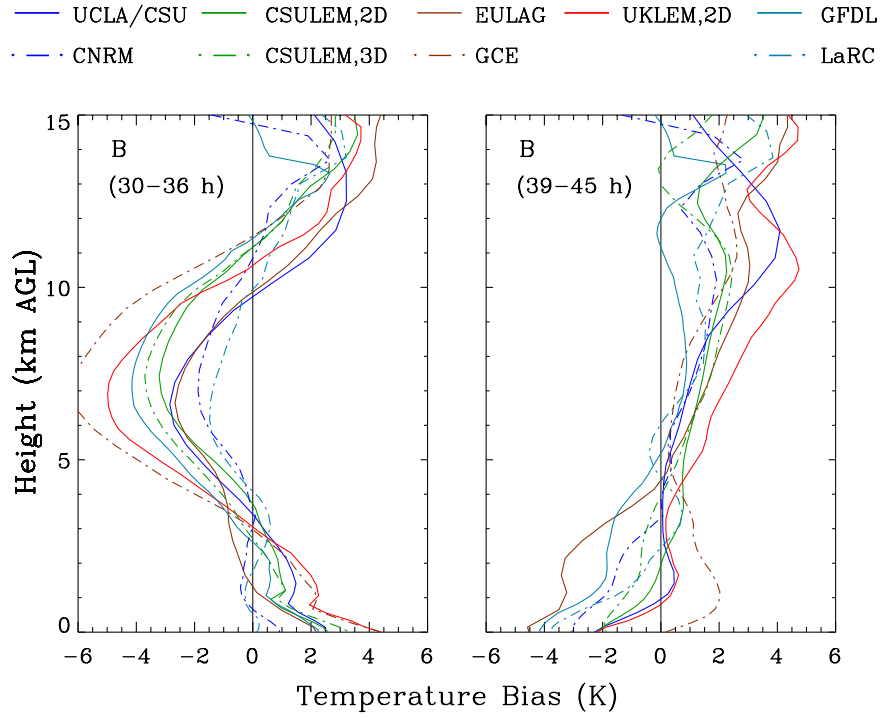
Fig. 4: Six-hour averaged temperature and water vapor mixing ratio biases for periods before (30 - 36 h) and after (39-45) the simulated precipitation peaks in Subcase B.

**Fig. 5:** The all-subcase mean errors of temperature and water vapor mixing ratio.
.

**Fig. 6**: Root-mean-square errors of temperature for Subcases A, B and C.
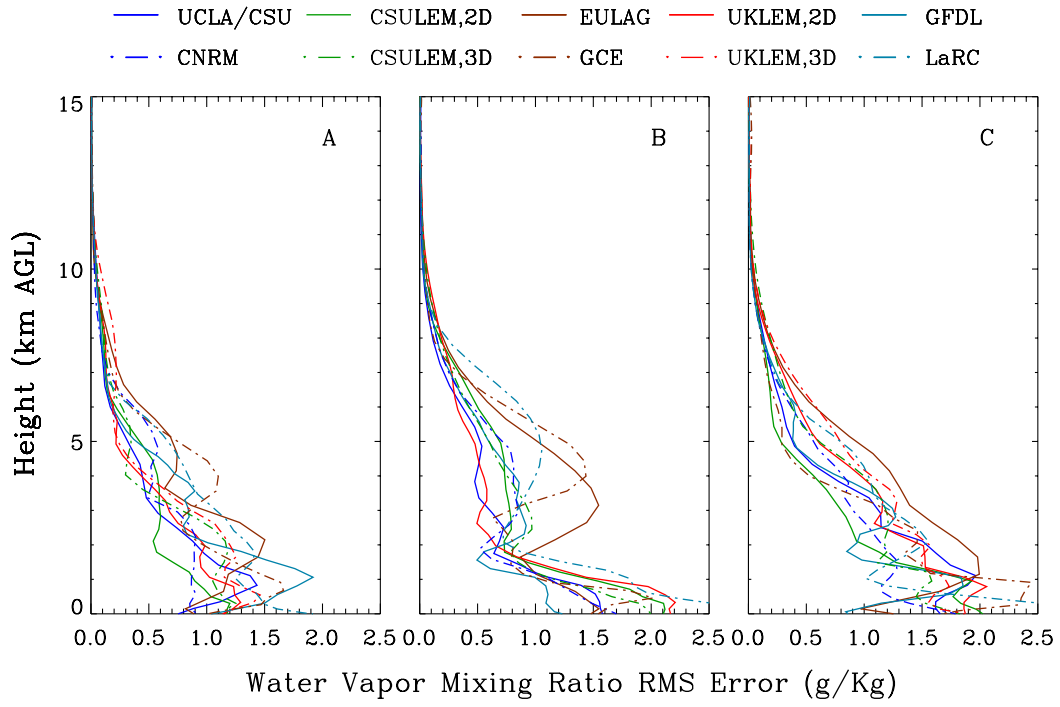
Fig. 7: Root-mean-square errors of water vapor mixing ratio for Subcases A, B and C.
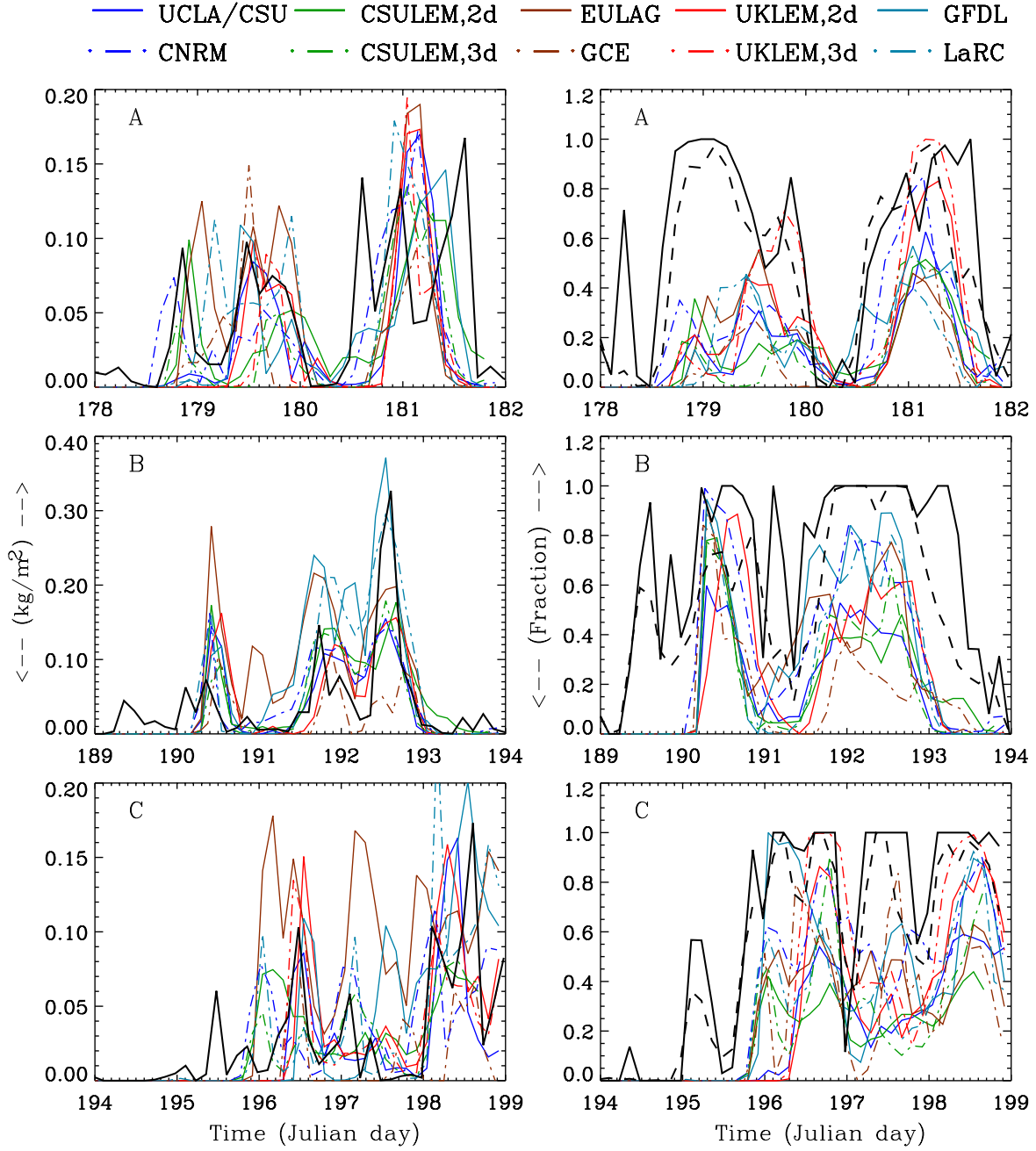
Fig. 8: Time series of observed and simulated cloud liquid water paths (left panels) and the column cloud fraction (right panels) for Subcases A, B and C. The black solid line on the left panels shows the MWR observations. The black solid and dashed lines on the right panels show the observations from MMCR and GOES, respectively.
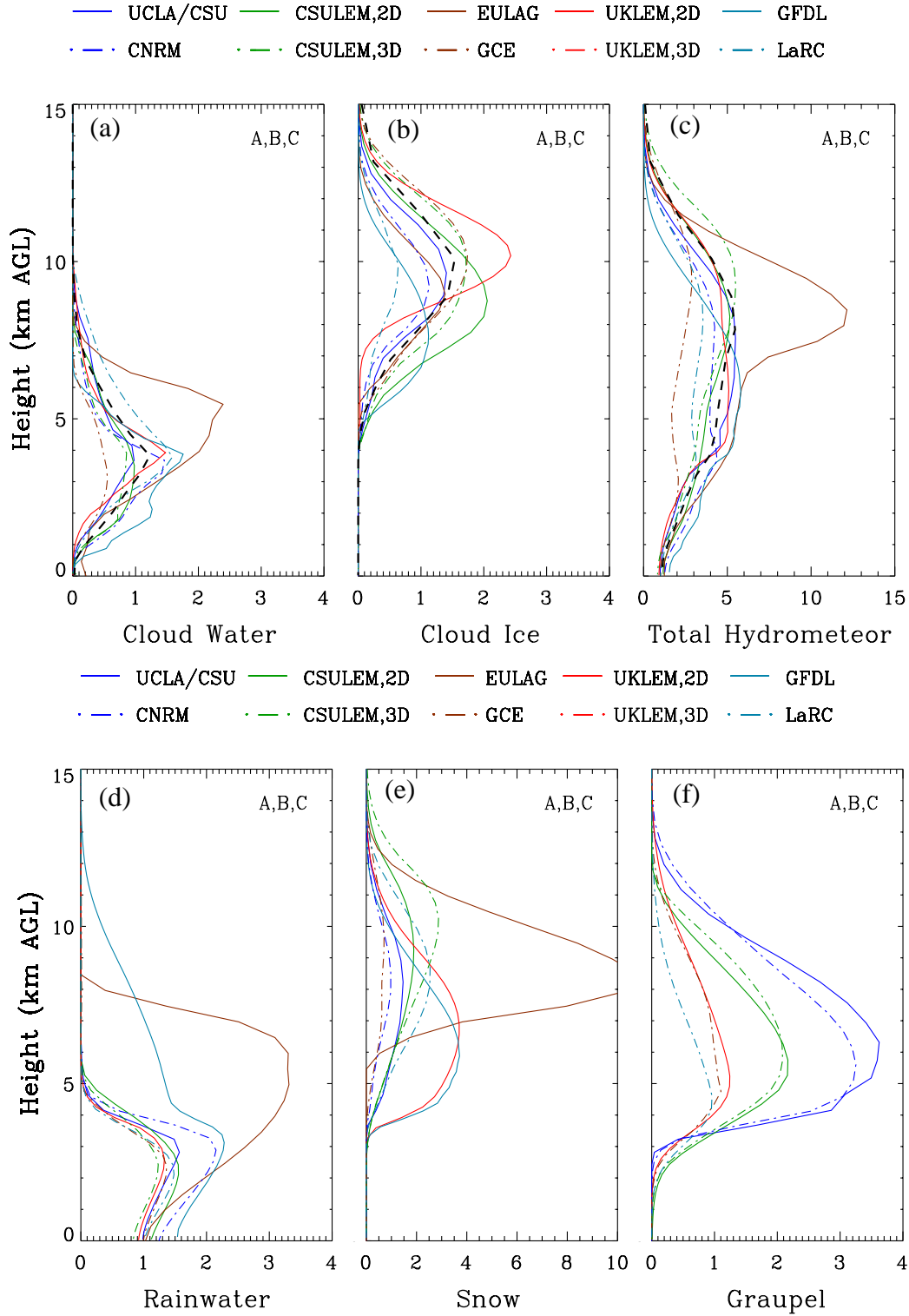
Fig. 9: The all-subcase mean profiles of the mixing ratios of (a) cloud water, (b) cloud ice (c) total hydrometeor, (d) rainwater, (e) snow and (f) graupel/hail. The black dashed line in (a), (b) and (c) shows the consensus of all models. Unit for the horizontal axes is $0.01 \, g \, kg^{-1}$. No observations is available for comparison.
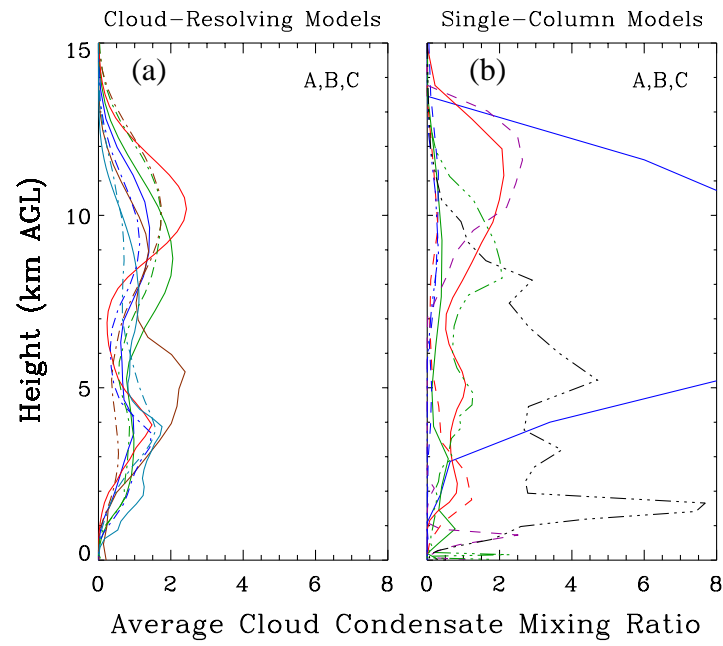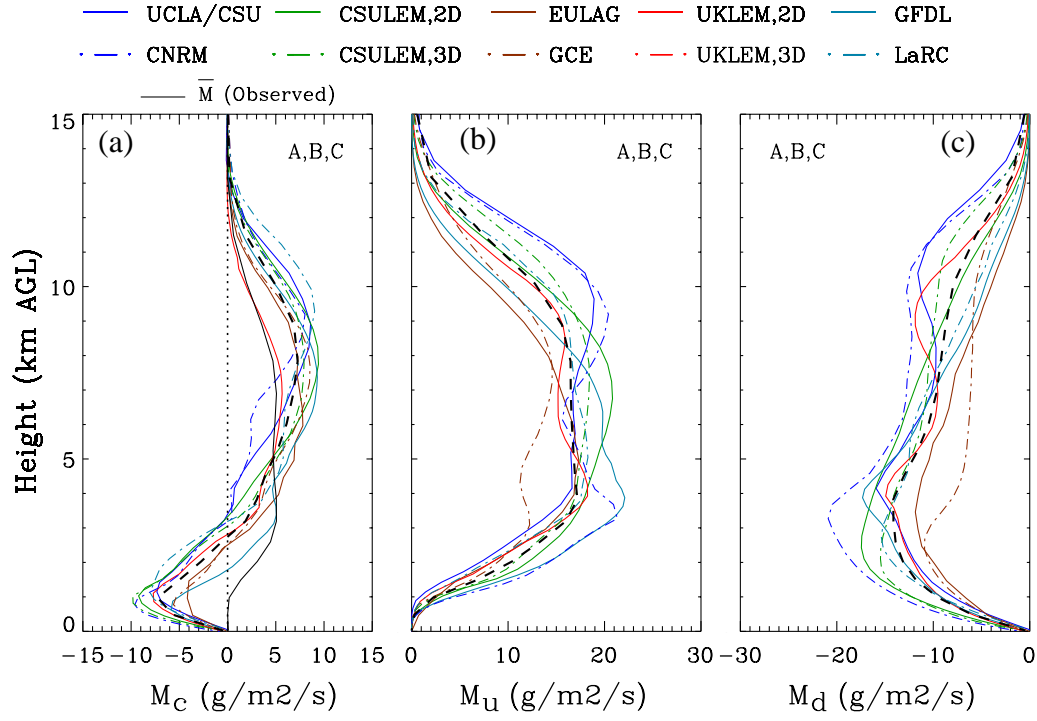
Fig. 10: Same as Fig. 9 except for the sum of cloud water and cloud ice mixing ratios for (a) CRMs and (b) SCMs. The legends of the CRM curves are identical to Fig. 9 but those for SCMs are not identified.
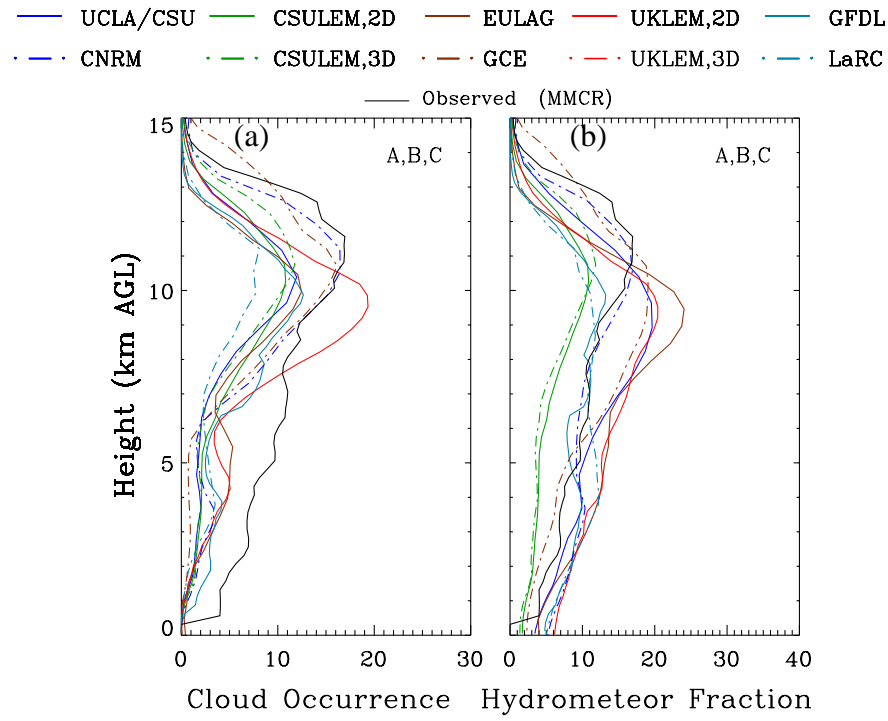
Fig. 11: Same as Fig. 9 except for cloud occurrence and hydrometeor fractions. Unit of the horizontal axes is percentage.

Fig. 12: Same as Fig. 9 except for cloud, updraft and downdraft mass fluxes. The thick black dashed line shows the consensus of all models.